## The role of surface oxygen vacancies in BiVO<sub>4</sub>

Wennie Wang,† Patrick James Strohbeen,‡ Dongho Lee,¶ Chenyu Zhou,§,∥ Jason Ken Kawasaki,‡ Kyoung-Shin Choi,¶ Mingzhao Liu,§ and Giulia Galli\*,†,⊥,#

†Pritzker School of Molecular Engineering, University of Chicago, Chicago, IL 60637, USA ‡Materials Science and Engineering, University of Wisconsin-Madison, Madison, WI 53706. USA

¶Department of Chemistry, University of Wisconsin-Madison, Madison, WI 53706, USA §Center for Functional Nanomaterials, Brookhaven National Laboratory, Upton, NY 11973, USA

|| Department of Materials Science and Chemical Engineering, Stony Brook University,
Stony Brook, NY 11794

⊥Materials Science Division and Center for Molecular Engineering, Argonne National

Laboratory, Lemont, Illinois 60439, USA

#Department of Chemistry, University of Chicago, Chicago, IL 60615, USA

E-mail: gagalli@uchicago.edu

#### Abstract

Bismuth vanadate (BiVO<sub>4</sub>) is a widely-studied oxide in solar water splitting, known for its ease of synthesis, high charge extraction yields, and advantageous band alignment with water. We present a combined first-principles and experimental study of the electronic structure of the (010) surface of BiVO<sub>4</sub> aimed at disentangling the impact of surface and bulk oxygen vacancies on the electronic structure and transport properties. We found that oxygen vacancies are deep donors at the surface as they are in the bulk; our calculations on defect and polaron formation energies suggest that while polarons

formed from oxygen vacancies in the bulk can contribute to conductivity, those at the surface likely do not. Our results also show that out-of-plane structural relaxations at the surface contribute to the relatively immobile nature of electron polarons derived from surface oxygen vacancies. The structural model derived from first-principles calculation was validated by comparing computed results with experimental measurements of single-crystal and epitaxially-grown single-crystalline BiVO<sub>4</sub> samples. We also found reasonably good agreement between our calculated and measured work functions for BiVO<sub>4</sub> samples with and without oxygen vacancies.

#### 1 Introduction

Solar water splitting is a renewable means for generating hydrogen fuel and a widely attractive avenue for clean energy.  $^{1-8}$  Hence the search for optimal photoelectrodes is an active field of research. At minimum an ideal photoelectrode should be stable in aqueous conditions, have a band gap in the visible, favorable band edge positions for water reduction and/or oxidation, and efficient electron-hole separation. n-type BiVO<sub>4</sub> has emerged as a promising material candidate that satisfies many of the aforementioned criteria for water splitting. BiVO<sub>4</sub> photoanodes are relatively inexpensive and facile to synthesize,  $^9$  in addition to being fairly stable against photoelectrochemical and chemical corrosion.  $^{9,10}$  Furthermore, the conduction band is closely aligned with the  $\rm H_2$  evolution potential.  $^{11-13}$  Perhaps most advantageous, as a photoanode BiVO<sub>4</sub> has a large (over 70%) electron-hole separation yield at a potential as low as 0.6 V vs reversible hydrogen electrode  $^{14}$  and a favorable photovoltage of  $\approx 1$  V for water oxidation.  $^{10}$  While the reported band gap (2.4-2.6 eV $^{11,14-16}$ ) is slightly too large to absorb a large fraction of the solar spectrum with high radiation flux,  $^{17}$  the band gap can be reduced via e.g., doping with nitrogen  $^{14}$  or pairing BiVO<sub>4</sub> with n-type semiconductors of smaller band gaps.  $^{18}$ 

Owing to these advantages, various efforts have been made to improve the photoelectrochemical behavior of BiVO<sub>4</sub>. <sup>14,19–24</sup> One such effort is to better understand the charge

transport properties. Conductivity in  $BiVO_4$  predominantly occurs through small polaron hopping,  $^{25-28}$  and the formation of small polarons is closely tied with that of oxygen vacancies, which are ubiquitous in oxides and can dramatically alter the electronic and atomic structure of the host solid. Consequently several studies have proposed various mechanisms in which oxygen vacancies may play a role in transport properties.  $^{14,20-22}$ 

Yet, the influence of polarons and oxygen vacancies on photoelectrochemical properties remains elusive. Whether the presence of oxygen vacancies hinders or helps the transport properties of BiVO<sub>4</sub> is still a controversial topic. For instance, Qiu et al. <sup>29</sup> reported better electron diffusivities and photocurrent densities for samples with lower oxygen vacancy concentration grown via electrodeposition. Qiu et al. attributed the improved conductivity in samples with lower oxygen vacancy concentration to the fact that oxygen vacancies may act as trap and recombination sites. In direct contrast, Zhang et al. <sup>30</sup> reported an improved electron conductivity for samples of higher oxygen vacancy concentration grown via pulsed laser deposition under a reducing carbon monoxide environment. These contrasting studies highlight the need to understand the role of oxygen vacancies in samples obtained from disparate growth and preparation methods.

In order to understand the microscopic role of defects on photoelectrochemical properties, we turn to computational studies. Several calculations have been carried out to characterize the pristine bulk in which no defects are present, including calculations of electronic structure and optical properties,  $^{12,31-34}$  transport properties,  $^{26,35}$  and electronic behavior of polarons in the bulk.  $^{36,37}$  For example, using hybrid functional molecular dynamics, Wiktor et al. found that at finite temperature the electron and hole polaron levels in the bulk are more than 1.0 eV from the  $\rm H^+/H_2$  and  $\rm H_2O/O_2$  redox potentials, respectively,  $^{37}$  suggesting favorable recombination of electron-hole polaron states. In the case of the defective bulk, computational studies have reported conflicting results on bulk oxygen vacancies, describing them as shallow centers in some density functional theory (DFT) studies  $^{38,39}$  and as deep centers in other DFT investigations with standard functionals  $^{20}$  and with hybrid functionals.  $^{21}$  Thus

far, these computational studies have mostly focused on the bulk or pristine surface.

However, the electronic structure and the morphology of photo-absorbing surfaces and interfacial chemistry naturally play a critical role in the photoelectrochemical activity. Different surface facets and terminations can have markedly varied chemistry and physics, e.g. they may act differently in separating the photon-generated electron-hole pairs. 40–42 Based on computed free-energy profiles of oxygen evolution reaction pathways and adsorption energies, 22,43 the presence of oxygen vacancies at the surface has been proposed to improve water splitting through increasing the number of active adsorption sites and potentially enhancing charge transfer. However, other studies have suggested that oxygen vacancies can primarily act as recombination centers and traps. 44 Investigations based on nudged elastic band calculations on oxygen migration suggested that vacancies mostly contribute to bulk conductivity. 45 Several computational studies have also considered the presence of water on BiVO<sub>4</sub> surfaces, either as adsorbed species, 46,47 as a frozen-liquid, 41,48 by both utilizing a solvation model 46 or an explicit solvent; 49 however, these studies assumed a pristine surface.

Despite an increasing number of insights coming from theory and computation, the role of oxygen vacancies in the bulk and at the surface of BiVO<sub>4</sub> remains controversial, and at best unclear. A systematic atomistic study on oxygen vacancies in relation to small polaron formation, particularly at the surface, appears to be essential to build a holistic understanding of the properties of BiVO<sub>4</sub> and thus achieve an efficient means towards generating clean hydrogen fuel. There are several open questions worth investigating: What is the level of first-principles theory needed to describe the surface of BiVO<sub>4</sub>? What is the role of surface relaxation? How do oxygen vacancies at the surface differ from those in the bulk (e.g., in polaron formation energy and charge states)? How do surface polarons differ from those in the bulk? How do we bridge the comparison between our calculations on single-crystalline structures and experimental photoelectrochemical devices based on polycrystalline materials? In this work, we aim to address these questions for the (010) BiVO<sub>4</sub> surface and provide the groundwork for future studies on interfaces with water. We focus on (010), which is one

of the most energetically favorable facets, for both epitaxial single-crystalline samples grown using the methodology from Refs. 27 and 30 and single crystals as previously reported in Ref. 11. We use first-principles methods and validate the structural model derived computationally by comparing calculated and experimentally-determined band edges and work functions. We compare our calculations with previously reported band alignment and work function measurements on single-crystalline samples <sup>11</sup> and with the work function we measured using single-crystalline epitaxial samples with a well-defined surface and composition. The epitaxial samples serve as a bridge between single-crystalline samples and polycrystalline samples that are used in devices, and ultimately in future studies will allow for more meaningful comparisons between our calculations and polycrystalline BiVO<sub>4</sub>.

The rest of the paper is organized as follows. The computational and experimental methodologies are presented in Sections 2 and 3, respectively. After introducing our results for the bulk in Section 4, we present an analysis on the structural relaxation of the pristing surface in Section 5. This is followed with band edge and work function calculations, with benchmarks using several levels of theory. We demonstrate that semi-local functionals have serendipitous agreement with experiment, and hybrid functionals are needed to accurately describe the band edges at finite temperature. We then introduce oxygen vacancies to the surface, investigating the stability of several surface polaron configurations and defect formation energies in Section 6. Our results indicate that a polaron arising from a surface oxygen vacancy is a deep donor whose electronic levels are well separated from the band edges and from the polaron levels at the pristine surface and in the bulk. Thus, unlike in the bulk, such defect polaron states are expected to contribute little to conductivity, but instead may serve as possible recombination centers. Next we compare work functions between single-crystalline epitaxially-grown samples and calculated slabs of BiVO<sub>4</sub> with and without oxygen vacancies. Finally, we conclude by discussing the broader impact of our results for the study of photo-electrochemical performance.

## 2 Computational Methodology

Our calculations are based on first-principles density functional theory (DFT) within the Kohn-Sham framework.  $^{50,51}$  We use a plane-wave basis sets and norm-conserving pseudo-potentials  $^{52,53}$  with a 90 Ry energy cutoff. The valence electrons are  $6p^36s^25d^{10}$ ,  $3d^34s^23p^63s^2$  and  $2p^42s^2$  for Bi, V and O, respectively. All bulk properties are obtained with a  $4 \times 4 \times 2$  k-point mesh; we verified that a larger mesh of  $6 \times 6 \times 4$  leads to < 0.5 meV difference in total energies. Forces on bulk structures are converged within 50 meV/Å. Our calculations were carried out with the QUANTUM ESPRESSO code.  $^{54,55}$ 

As BiVO<sub>4</sub> is non-magnetic, we use DFT+U<sub>eff</sub><sup>56</sup> with U<sub>eff</sub> = (U-J) = 2.7 eV applied to the vanadium 3d states.<sup>57</sup> This value of U was previously tested for bulk BiVO<sub>4</sub>.<sup>14,21</sup> We also used the dielectric-dependent hybrid (DDH) functional as described in Ref. 58, which showed DDH yields more robust band gaps across several elemental and binary compounds compared to the general gradient approximation and hybrid functionals with standard mixing  $\alpha = 0.25$ . In DDH, the Hartree-Fock mixing parameter  $\alpha = 1/\varepsilon_{\infty} = 1/6.9 = 0.145$  equals the inverse of the high-frequency dielectric constant, <sup>14,21</sup> obtained using density functional perturbation theory. A comparison of our calculated bulk parameters with those reported in the literature may be found in the Supplementary Information (SI).

While several choices of surface cleavage are possible, we focus on the lowest energy surface. We generated symmetric slabs<sup>59</sup> using a 24-atom I2/b cell with tetragonal lattice parameters, which is related to the conventional monoclinic C2/c cell via a change-of-basis transformation.<sup>9</sup> Each slab consists of at least 20 Å of vacuum and a minimum of 8 atomic layers (see SI for convergence tests). Previous reports<sup>21</sup> have found the monoclinic and tetragonal lattice parameters yield comparable defect electronic structure and formation energies in the bulk. Similarly we find that using tetragonal lattice parameters is a reasonable approximation to the monoclinic cell for slab calculations; the computed band gaps differ by < 0.05 eV, the work function by < 0.1 eV, and band edges by < 0.05 eV. In the C2/c cell, the lowest energy surface is the (010) plane (equivalent to the (001) surface in the I2/b cell).

We henceforth refer to this surface as the (010) surface.

In order to simulate the presence of an oxygen vacancy at the surface, an oxygen atom is removed within the first two layers from the surface (see Section 5) of a  $2 \times 2 \times 2$  slab supercell and calculated with a  $2 \times 2 \times 1$  k-point mesh. In the case of Mo-doping considered for comparison with work function measurements, we substitute one V for Mo for each atomic percent concentration. We verified that a  $4 \times 4 \times 1$  k-point mesh leads to total energy differences on the order of 1 meV. Spin polarization is included in our calculations and all defect or slab geometry forces are converged to within 100 meV/Å.

#### 2.1 Defect Formation Energies

We calculate the defect formation energy for oxygen vacancies near the surface in order to investigate their thermodynamic stability and compare with their corresponding properties in the bulk. The formation energy of an oxygen vacancy is defined as <sup>60</sup>

$$E^f[V_O] = E_{\text{tot}}[V_O^q] - E_{\text{tot}}[\text{BiVO}_4] - \mu_O + qE_F + \Delta^q, \tag{1}$$

where  $E_{\text{tot}}[V_{\text{O}}^q]$  is the total energy of a slab supercell containing the oxygen vacancy,  $E_{\text{tot}}[\text{BiVO}_4]$  is the total energy of the pristine slab, and  $\mu_{\text{O}}$  is the chemical potential of oxygen. The Fermi level  $E_F$  is referenced to the valence-band maximum (VBM) of the bulk. The term  $\Delta^q$  is a charge-state dependent correction due to the finite size of the supercell,  $^{60}$  which allows for the extraction of the defect properties in the dilute limit. We follow the method proposed by Freysoldt et al.  $^{61}$  to compute the  $\Delta^q$  in two-dimensional systems. Further discussion on the calculated chemical potentials and comparison of our calculated heat of formation enthalpies with literature and experimental results may be found in the SI.

## 3 Experimental Methodology

Epitaxial BiVO<sub>4</sub> thin films with (010)-orientation (with respect to the C2/c cell) are grown by pulsed laser deposition (PLD) over (001) yttria-stabilized zirconia (cubic, a = 5.145 Å) substrates with an epitaxial indium tin oxide (cubic, a = 10.127 Å) buffer layer as the bottom electrical contact, at conditions similar to those of Refs. 28 and 27. We prepared undoped asgrown epitaxial samples in which the laser ablation target is made of stoichiometric BiVO<sub>4</sub>. Measurement details on the photo-emission spectroscopy and work function determination are provided in the SI.

## 4 Bulk Properties

We begin with a brief description of the bulk properties computed at three levels of theory: semi-local density functional theory (DFT), DFT+U, and dielectric-dependent hybrid functionals (DDH<sup>58</sup>). As shown in Figure 1, the crystal structure of BiVO<sub>4</sub> consists of 4-fold tetrahedrally coordinated vanadium atoms, which are corner-sharing with 8-fold dodecahedrally coordinated bismuth atoms. The bulk electronic properties have been studied at great length, <sup>11,12,32,62</sup> and here we highlight key features. The bulk V-O bond length is 1.74 Å in DFT+U (1.72 Å in DDH); the bulk Bi-O lengths range between 2.51 and 2.45 Å (2.44 and 2.49 Å in DDH).

Similar to many other transition metal oxides, the occupied electronic states of BiVO<sub>4</sub> have predominantly O 2p character whereas the unoccupied states have mostly transition metal character, i.e, V 3d. Salient features are the non-negligible contribution of the Bi p orbitals to the conduction bands and the s-character at the top of the valence states arising from the lone pair on Bi, which is frequently invoked to have a key role in photo-electrochemical activity. <sup>16,63,64</sup> The relative position of electronic states stemming from Bi, V, and O as found in our calculations has been corroborated extensively with molecular orbital theory <sup>32</sup> and near edge x-ray absorption fine structure measurements (NEXAFS). <sup>11</sup>

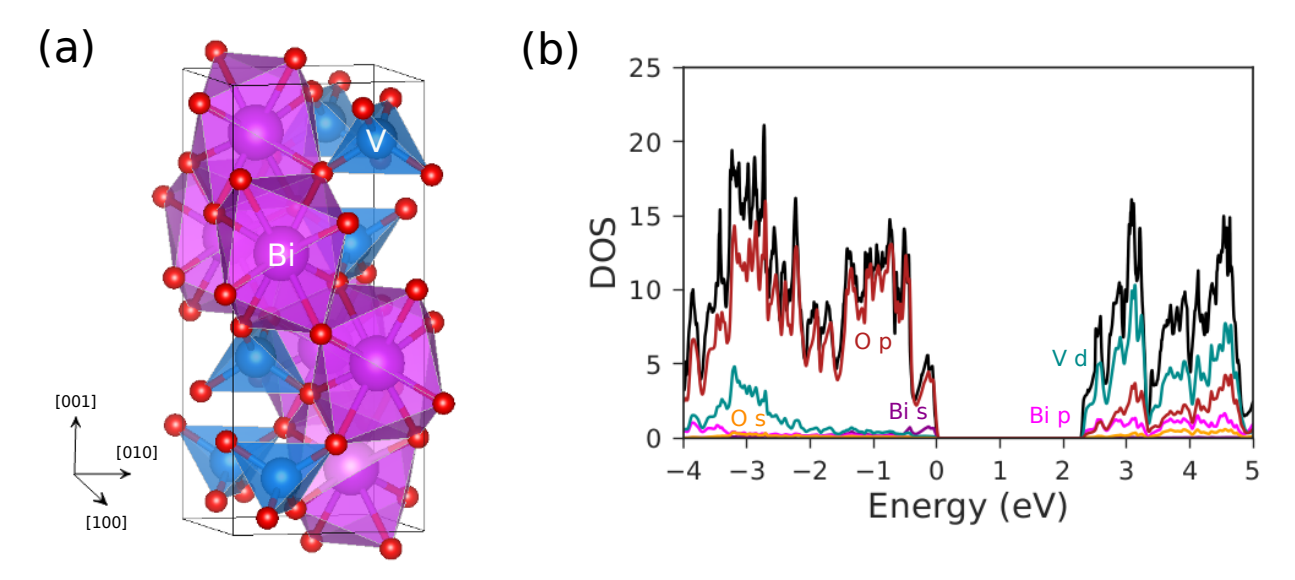


Figure 1: (a) Crystal structure of  $BiVO_4$  with bismuth atoms in purple, vanadium atoms in blue, and oxygen atoms in red. (b) The corresponding total (black) and projected (colored) density of states. The valence band maximum is referenced to zero.

A detailed summary of bulk lattice parameters and band gaps may be found in the SI. Overall, there is fair agreement between calculated lattice parameters at the DFT, DFT+U and DDH levels of theory with at most 0.8% error relative to experiment. Interestingly, the DDH lattice parameters computed at T=0 appear to exhibit the largest error, when compared to experiment. However, as discussed below, this is likely due to significant temperature renormalization effects.

The fundamental band gap (defined as the difference between the conduction and valence band edges) at the DFT+U level is  $\sim 2.27$  eV (3.44 eV in DDH), which is an apparent underestimation (large overestimation in DDH) of the experimental value ( $\sim 2.4$ -2.6 eV<sup>11,14–16</sup>) (see SI). However, it is known that temperature renormalization (which is not captured in our 0 K DFT calculations) is significant. Using path-integral molecular dynamics simulations (PIMD), Wiktor et al.<sup>34</sup> evaluated the total renormalization of the fundamental band gap at room temperature [including spin-orbit coupling (SOC), which comes primarily from Bi and lowers the band gap by 0.13 eV]; they reported values of 0.70 eV for semilocal functionals and 1.05 eV for PBE0. While a finite temperature study is beyond the scope of this paper,

in Section 5.2 we shall use a rigid band shift as an ad-hoc correction to demonstrate the influence of temperature corrections on band alignment.

## 5 Pristine (010) Surface

#### 5.1 Surface relaxation

We now consider the cleaved (010) surface (equivalent to the (001) plane in our I2/b cell) terminated by fully-coordinated vanadium atoms and 6-fold coordinated bismuth atoms. As mentioned earlier, the (010) surface has one of the lowest calculated surface energies.  $^{32,65}$  Since epitaxial single-crystalline samples can be grown and single-crystalline samples can be cleaved along the (010) surface, we can make direct comparisons between our calculations and experiment. As mentioned in the Introduction, we use our single-crystalline epitaxial samples as a point of comparison and bridge between single-crystalline (ideal electrode) and polycrystalline samples (actual electrode used in devices).

Allowing our slab calculations to relax results in a (1x1) surface reconstruction, as shown in Figure 2(a) and (b), which agrees with low energy electron diffraction (LEED) measurements on single-crystalline samples. <sup>11</sup> In the first layer from the surface, the exposed V-O groups contract by  $\sim 3.4\%$  for the bonds pointing towards the vacuum but elongate by  $\sim 4.8\%$  for those pointing towards the bulk. A 2.2% elongation of the Bi-O bond length complements the relaxation for the bonds pointing towards the vacuum, with up to 6.1% contraction for bonds pointing towards the bulk. This is accompanied by a small increase in relative displacement along z between the V and Bi (on the order of 0.04 Å). In the second layer, the reverse occurs; that is, V-O bonds elongate by 2.5% for bonds pointing towards the vacuum but contract by 1.5% for bonds pointing towards the bulk. Conversely, the Bi-O bonds contract by 3.5% for bonds pointing to the vacuum and elongate by 1.9% for those pointing towards the bulk. By the third layer from the surface, the V-O and Bi-O have essentially returned to their bulk bond lengths. A histogram detailing the change in V-O and

Bi-O bond lengths is given in Figure 2(c). An important consequence of this relaxation in the (010) surface is the observation of facet-dependent accumulation of carriers as explained below.

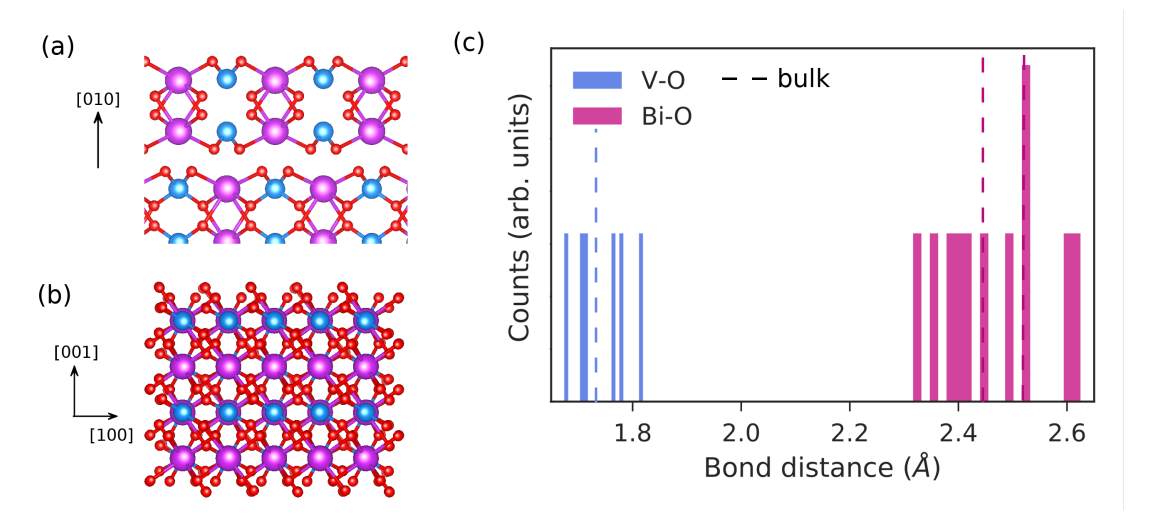


Figure 2: (a) Side and (b) top view of the relaxed (010) surface in BiVO<sub>4</sub>. To illustrate the pattern of surface relaxations, only V-O bonds less than the bulk bond length of 1.74 Å and Bi-O bonds less than 2.55 Å are shown. (c) The corresponding histogram distribution of the V-O and Bi-O bond lengths within the first three layers of the surface; bulk bond lengths are shown as dashed lines.

In order to extract band edges and the work function, we align computed eigenvalues to the vacuum level using the electrostatic potential, which consists of the bare ion and Hartree potential. The electrostatic potential is averaged within the plane for each atomic layer to obtain the microscopic potential and then averaged again out of the plane to yield the macroscopic potential. An example is shown in Figure 3. As a result of the structural relaxation described previously, a potential well emerges in the average electrostatic potential  $\tilde{V}$  that results in an accumulation of electrons. A similar potential well feature occurs at the DDH level (see SI). This is consistent with experiments that suggest certain facets have preferential accumulation of electrons.  $^{41,42,66,67}$  For instance, deducing from the growth patterns of photo-deposition of dual precursors, Li et al.  $^{42}$  demonstrated that the  $\{010\}$  facet prefers reduction reactions, which suggests electron accumulation. Similarly, Tachikawa et al.  $^{66}$  used potential-induced spatially-resolved photoluminescence emission to show other low-

index facets instead prefer hole accumulation. We discuss the impact of surface relaxation on the formation of small polarons in Section 6.

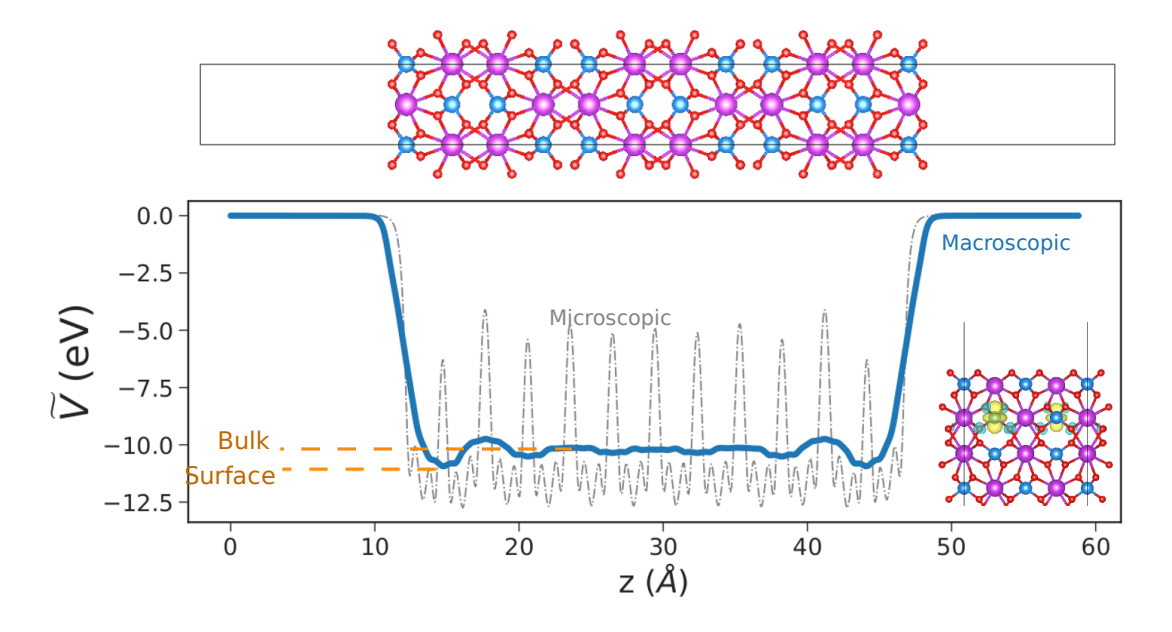


Figure 3: Microscopic and macroscopic average electrostatic potential  $\tilde{V}$  of the (010) slab obtained using DFT+U. The orange dashed lines indicate the potential at the surface and in the bulk averaged along the z direction. The surface  $\tilde{V}$  is 0.68 eV below that of the bulk. This potential leads to electron accumulation, as shown in charge density inset displaying the spin-polarization (defined as the difference in spin up and spin down charge densities,  $\Delta \rho = \rho_{\rm up} - \rho_{\rm down}$ ; yellow is positive  $\Delta \rho$  and blue is negative  $\Delta \rho$ ) for an extra electron in the pristine slab.

### 5.2 Band alignment

Next we compare our slab calculations with band alignment measurements on previously reported single-crystalline samples from Ref. 11 to evaluate the accuracy of our structural models. Figure 4 shows a direct comparison between theory and experiment on the absolute position of the band edges with respect to vacuum, along with the standard hydrogen and oxygen redox potentials.

Similar to the band gap, there is a serendipitous agreement in band alignment between DFT+U at T=0 and experiment, with differences  $\sim 0.2$  eV. Indeed, temperature renormalization plays an important role in the absolute position of the bands. We can make

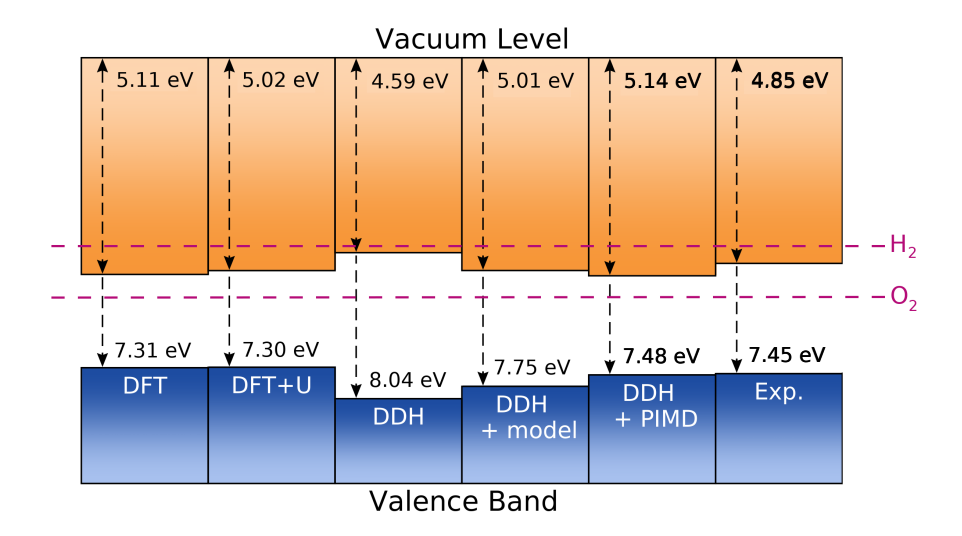


Figure 4: Band alignments for BiVO<sub>4</sub> at DFT, DFT+U, DDH<sup>58</sup> levels of theory as referenced to the vacuum. Two estimates for temperature renormalization are given: (DFT+model) based on the equations from Ref. 68 and (DFT+PIMD) from the results of Ref. 34. Single-crystalline experimental measurements are taken from Ref. 11. For convenience, the hydrogen and oxygen redox potentials are given as dotted lines. See text and SI for further details. Generated with bapt, https://github.com/utf/bapt.

two estimates on the effect of temperature, involving a rigid shift in the band edge using 1) values calculated with path-integral molecular dynamics (PIMD)<sup>34</sup> and 2) values based on Rayleigh-Schrödinger perturbation theory for electron-optical phonon interactions<sup>68</sup> (see SI for calculation details). Using a screened hydrogenic model, the exciton binding energy is estimated to be  $\sim 0.18$  eV, which is a slight overestimate to the value derived from explicit calculations based on GW quasiparticle eigenvalue shifts (0.11 eV<sup>34</sup>). Using method 1), the combined renormalization from nuclear quantum effects and finite temperature is  $\Delta VB \approx 0.56$  and  $\Delta CB \approx -0.36$  eV (using PBE0). Spin-orbit coupling leads to primarily a lowering of the conduction band states. Adding spin-orbit coupling and excitonic effects, we obtain  $\Delta VB \approx 0.61$  and  $\Delta CB \approx -0.54$  eV. For method 2), we estimate  $\Delta VB \approx 0.29$  and  $\Delta CB \approx -0.42$  eV, where spin-orbit coupling and the excitonic binding energy calculated from the hydrogenic model are included. As Figure 4 illustrates, when these corrections are included, the agreement between experiment and DDH improves whereas DFT+U at T=0 provides accidental agreement to the correct band alignment. Thus, a finite-temperature

study of interfacial and surface phenomena in BiVO<sub>4</sub> requires at minimum an hybrid functional level of theory to provide an accurate description. Studies on other oxides like WO<sub>3</sub> similarly find strong temperature renormalization effects. <sup>69</sup> Nevertheless, as demonstrated in Refs. 21 and 45, DFT+U qualitatively agrees with DDH calculations for explaining major trends in the electronic structure, formation energies, and polaron formation related to the oxygen vacancy. Thus, below we use DFT+U to characterize the substoichiometric surface, focusing on trends.

## 6 Substoichiometric (010) Surface

#### 6.1 Formation of polarons

In general, the formation of an electron polaron involves the localization of an electron on an atomic site; in the case of  $BiVO_4$ , the polaron self-traps on the vanadium sites, changing the nominal  $V^{5+}$  charge state to  $V^{4+}$ . We distinguish between three cases: 1) an extra electron is introduced in the pristine structure and it is delocalized instead of forming a polaron, 2) an extra electron is introduced in the pristine structure and it localizes to form a polaron, 3) an oxygen vacancy is introduced and the associated electron(s) localize nearby to form polarons. We define the polaron binding energy as the total energy difference between 1) and 2). The energy difference between the level in the band gap corresponding to 2) and defect charge-transition level of 3) is defined as the ionization energy of a defect polaron with respect to a polaron far from the defect. This is different from the ionization energy defined with respect to the conduction band minimum, and it is the former that is important to consider in studying polaron hopping. In Section 6.2, we further distinguish between polarons formed at the surface and in the bulk.

We first note that when an extra electron is introduced to the pristine surface, it can be stabilized as a polaron, as in the case of an extra electron introduced in the bulk.<sup>37</sup> We calculated the polaron binding energy to be 0.12 eV for the surface, compared to 0.52 eV in

the bulk.<sup>14</sup> This suggests that electron polarons tend to occur in the pristine bulk rather than the pristine surface. Wiktor et al.<sup>36,37</sup> similarly find the surface polaron has a 0.4 eV smaller binding energy compared to the bulk polaron for the pristine bulk and pristine surface at finite temperature (0.18 eV smaller in the presence of water).

Next, we introduced oxygen vacancies and we present a comparison of the oxygen vacancy formed in the bulk $^{21}$  and at the surface and of the accompanying formation of small polarons. We calculated surface polaron configurations analogous to those in the bulk (see Ref. 21), adopting similar naming conventions. Electron polaron formation in BiVO<sub>4</sub> is accompanied by an expansion of V-O bond lengths. At the surface, this is as much as 4.4%. Figure 5 presents the spin-polarized charge densities of each of these configurations and their relative stabilities for the neutral oxygen vacancy where two excess electrons are left behind. For each configuration, we initialize the relaxed pristine surface structure to favor polaron formation at a specific V site through 1) inducing a slight expansion ( $\sim 3\%$ ) of V-O bond lengths and 2) inducing a finite magnetic moment in the spin-up configuration at specified sites; then, we label these configurations by C1 through C6 and allow each configuration to relax. Configurations C1-C4 involve localization of electrons on the VO<sub>3</sub> polyhedron containing the defect site. In configurations C2-C6, the structure is modified in such a way that the VO<sub>3</sub> polyhedron shares an oxygen of a neighboring VO<sub>4</sub> one layer below the exposed surface. In other possible configurations, C3, C5, and C6 involve localization on either a neighboring corner-sharing  $VO_4$  or a  $VO_4$  in the proximity.

Each of these configurations were triplet states (S=1); as in the bulk, the triplet is slightly more stable than the singlet (by about 30.7 meV at the surface using DFT+U). At the surface, configurations where the VO<sub>3</sub> polyhedron distorts to share an O corner with a neighboring VO<sub>4</sub> tetrahedron are energetically favored, much like in the bulk. The lowest polaron formation C5 is favored by approximately 650 meV compared to C1, which is markedly smaller than the largest relative energy differences in the bulk (nearly 800 meV). In general, a self-trapped electron is accompanied by a local expansion of the lattice, in this

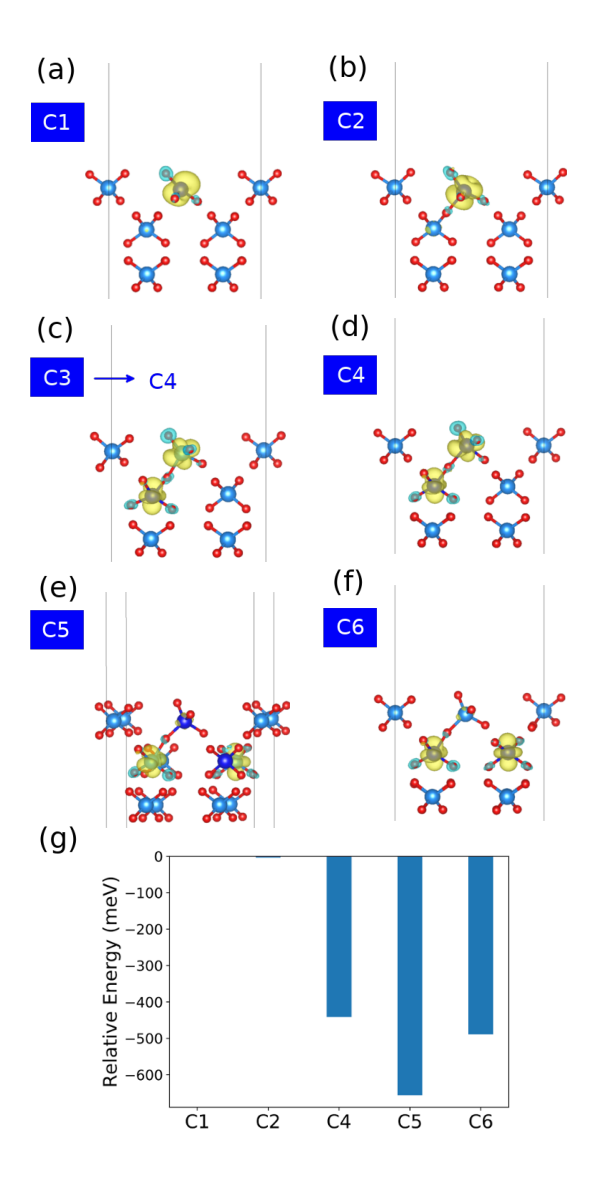


Figure 5: Possible configurations for small polaron formation near an oxygen vacancy  $V_{\rm O}$  at the (010) surface of BiVO<sub>4</sub> (a-f) and (g) corresponding relative total energies with respect to the first configuration (C1) obtained using DFT+U. Bi atoms are omitted for clarity. Oxygen atoms are represented in red; V atoms are blue and darker colored V indicate sites of initial polaron formation before relaxation. The spin-polarization (defined as the difference in spin up and spin down charge densities,  $\Delta \rho = \rho_{\rm up} - \rho_{\rm down}$ ) of the relaxed structure is shown in yellow (positive  $\Delta \rho$ ) and blue (negative  $\Delta \rho$ ). (a) Two electrons donated by the  $V_{\rm O}$  localize entirely at the defect site at the surface. (b-f) The VO<sub>3</sub> polyhedron containing the  $V_{\rm O}$  shares an O with a neighboring VO<sub>4</sub>. (b) Both electrons localize at defect site. (c) Both electrons initialized to localize on a corner-sharing VO<sub>4</sub>, but relaxes to C4. (d) Each electron localizes on the surface VO<sub>3</sub> and a corner-sharing VO<sub>4</sub>. (e) Despite being configured towards charge localization on the VO<sub>3</sub> polyhedron and a neighboring VO<sub>4</sub>, the relaxed configuration results in polarons on the corner-sharing VO<sub>4</sub> and a separate VO<sub>4</sub>. (f) An electron localizes at the corner-sharing VO<sub>4</sub> and a separate VO<sub>4</sub> near the surface.

case the V-O bonds in a vanadium-centered polyhedron. The formation of a surface polaron must thus compete with existing surface relaxations consisting of alternating bond length contractions and elongations, as described in Section 5.1, and thus leads to a higher energetic cost in lattice strain. Hence, the surface polaron in the presence of an oxygen vacancy tends to form in the second layer from the surface where surface relaxations are smaller (e.g., C4 through C6). Nevertheless, the formation of electron polarons near the oxygen vacancy is favorable at the surface, as it is in the bulk.

#### 6.2 Defect Formation Energies

Oxygen vacancies are n-type defects that in principle can take on 0, 1+, or 2+ charge states. In order to understand the thermodynamic stability of forming an oxygen vacancy, we calculate the formation energy and compare it with the corresponding one in the bulk. This comparison is shown as Figure 6 at the DFT+U level. In the bulk,  $^{21}$  the oxygen vacancy can take on +2, +1, and neutral charge states. The charge-transition level (CTL) for (+1/2+) is reported to be 0.87 eV and for (1+/0) as 0.59 eV below the conduction band minimum (CBM).  $^{21}$  Thus, the oxygen vacancy in the bulk is a deep donor with an ionization energy of 0.59 eV with respect to the conduction band minimum. However, the ionization energy with respect to a small polaron in the pristine bulk away from the oxygen vacancy is on the order of 0.21 eV (at DDH it is 0.11 eV). At finite temperature, this energy difference is expected to be small enough so that the polaron formed from oxygen vacancies in the bulk can contribute to conductivity via polaron hopping. This is consistent with experimental measurements on mobility that indicate thermally activated small polaron hopping to be the dominant conduction mechanism at room temperature (at lower temperatures variable polaron hopping is reported as the dominant contributor to conductivity instead).  $^{25,70}$ 

In contrast, the surface oxygen vacancy is predominantly stable as the +1 and neutral charge states for most values of the Fermi level in the band gap. The fact that the +2 charge state is found to be less stable at the surface than in the bulk may be related to surface

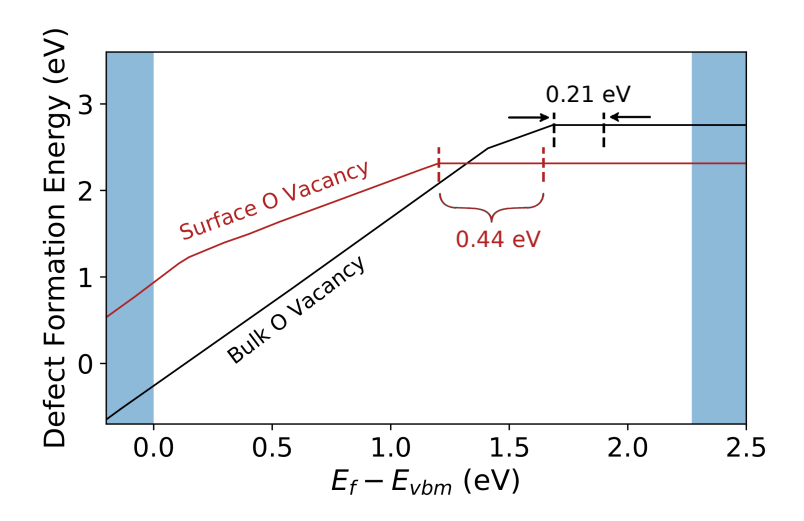


Figure 6: Comparison of defect formation energies of the surface and bulk oxygen vacancy under oxygen-rich conditions as a function of the Fermi level  $E_f$  position obtained using DFT+U. The slope of each curve corresponds to the charge state of the defect with intersections corresponding to charge-transition levels (CTL). These curves represent the lowest energy configuration. The band edges are shown with shaded blue areas. The black dotted lines indicate energy difference between the (+1/0) CTL and the polaron level in bulk BiVO<sub>4</sub>, i.e., the ionization energy of the neutral oxygen vacancy to polaron level is 0.21 eV. That difference is 0.44 eV between the neutral surface oxygen vacancy CTL and surface polaron level, as indicated by the red dotted lines. Bulk oxygen vacancy formation energies are from Ref. 21.

relaxations, which tend to create a potential well that attracts electrons, as discussed in Section 5.1. The (1+/0) CTL for the surface defect is significantly deeper than that in the bulk, at 1.07 eV below the CBM, indicating that the neutral oxygen vacancy is the dominant charge state for most values of interest for the Fermi level position. As with the bulk, we calculated the difference between the (+1/0) CTL to the level associated with an electron polaron at the pristine surface, and find an energy difference of 0.44 eV. Even at finite temperature (e.g., ambient conditions), this barrier would be unfavorable for polaron hopping compared to the bulk; thus, we do not expect surface polarons from oxygen vacancies to contribute significantly to mobility.

We note that our calculated formation energies are up to 1 eV smaller than those reported in Ref. 45, which may be due to their use of the PBEsol functional as well as different choices of the simulation cell. Hegner et al<sup>45</sup> use a 6-layer slab (compared to our 8-layer slab),

which exhibits uneven relaxation and has no effective bulk region, as surface relaxations occur throughout the slab. For the tetragonal structures relaxed with PBEsol, the in-plane lattice parameters are a = 5.117 and c = 11.587 Å. <sup>45</sup> Our calculated lattice parameters for the tetragonal cell with PBE+U are a = 5.172 and c = 11.770 Å. We note that our lattice parameters are in better agreement with measured BiVO<sub>4</sub> lattice parameters (see comparison with experiment in Table S3 of SI) and hence the local bonding environment, which plays an important role in charge localization.

# 7 Variation of work function with oxygen vacancy concentration

We next calculate the variation of the work function  $\varphi$  with oxygen vacancy concentration and compare with experiment. Oxygen atoms are removed from each exposed surface within the first two layers from the surface in incremental amounts. Effectively this amounts to removing two oxygen atoms per 1 at% in our  $2 \times 2 \times 2$  192-atom supercell (where at% is defined with respect to the total number of atoms). Table 1 lists our calculated work function  $\varphi$  as a function of oxygen vacancy. The corresponding density of states are presented in the SI. Not surprisingly for an n-type defect, a higher oxygen vacancy concentration results in a lower work function (i.e., higher Fermi level). Overall, our calculations suggest the work function can decrease up to 0.7 eV for up to 5 at% oxygen vacancy concentration.

We next compare our calculated work function values with those in the literature. We note that our calculated work functions are lower by up to 1 eV compared to other computational studies.  $^{41,45}$  We find that a higher calculated work function can arise from a poorer sampling of the Brillouin zone in the calculation of the density of states from which the Fermi level is determined. Our work functions are calculated to within 0.02 eV computational accuracy with respect to k-point sampling; further details are provided in the SI, including comparison with literature values. When comparing with measured work functions (e.g., as

done in Ref. 45), we note that caution must be taken, as the work function can be highly sensitive to surface features, surface defects, and surface contaminants. <sup>12,71,72</sup> For example, Hermans et al<sup>71,72</sup> deposited polycrystalline BiVO<sub>4</sub> thin films interfaced with various oxides using pulsed laser deposition and measured work functions that range between 5.6 eV to 6.6 eV. In another study, Cooper et al<sup>12</sup> grew polycrystalline thin films with chemical vapor deposition and measured a work function of 5.27 eV. These studies illustrate the sensitivity of work functions to polycrystallinity, sample preparation procedure, and surface and/or interfacial effects. Hence, because of differences in sample preparation and unclear sample stoichiometries, it is challenging and delicate to make a one-to-one comparison between calculated and measured work functions.

Here, in order to validate the level of theory we used to calculate the work function, we compare with the measured work function reported in Ref. 11, where Czolchralski-grown stoichiometric single-crystalline samples were used. These measurements remove any uncertainties introduced by polycrystallinity or interfacial effects. Furthermore, the level of surface contaminants was found to be below detectable levels in x-ray photoelectron spectroscopy measurements. Since undoped single-crystalline samples are too insulating for reliable measurements,  $\sim 1$  at% Mo-doping was used to improve sample conductivity. The measured relative stoichiometry was reported to be Mo<sub>0.02</sub>:Bi<sub>1.09</sub>V<sub>1.00</sub>O<sub>4.04</sub>, which is within the nominal 1 at% Mo-doping stoichiometry of Mo<sub>0.06</sub>:Bi<sub>1.00</sub>V<sub>1.00</sub>O<sub>4.00</sub> when considering instrument detection limits. 11 Favaro et al 11 measured a work function of 5.15 eV. In order to better compare with this sample, we calculate the work function with 1 at \% Mo-doping. Our calculations suggest that 1 at % Mo-doping can lead to comparable decreases in the work function as that of 1 at% oxygen vacancies ( $\varphi \sim 4.9$  eV). The measured work function of 5.15 eV is within the range of our calculated work functions for the pristine and 1 at Mo-doped slabs (5.40 eV and 4.86 eV, respectively). The fact that the measured work function is somewhat larger than the calculated work function for 1 at Mo-doping is reasonable considering that the measured stoichiometry has a smaller Mo concentration compared to the nominal

stoichiometry. This agreement further validates our structural model and methodology.

Table 1: Calculated work function  $\varphi$  for Mo-doping and various concentrations of oxygen vacancies using DFT+U. Labels correspond to the number of defects present per exposed surface; each removed oxygen or substituted Mo corresponds to 1 at%.

Config.	$\varphi$ (eV)
pristine	5.401
$1 \text{ Mo}_{V}$	4.906
$1 V_{\rm O}$	4.861
$5 V_{\rm O}$	4.670

Next, in order to validate whether our calculated work function as a function of surface oxygen vacancy concentration on the (010) surface is reasonable, we measured the work function of the (010) plane of epitaxially-grown single-crystalline samples. The surface of these samples is expected to be well defined and significantly more uniform than typical polycrystalline samples having randomly oriented grains with varying defect levels. Thus, this sample is appropriate to validate our calculations. The work function of this sample was determined using ultraviolet photoemission spectroscopy (UPS). Further details on the experimental set up and analysis procedure for accurately measuring the work function are provided in the SI.

The surface oxygen vacancy concentration on the (010) plane of the epitaxially-grown single crystalline samples were determined by quantitative analysis of the V  $2p_{3/2}$  peaks of the x-ray photoelectron spectra, which is sensitive only to the surface composition. Ideally on average, each oxygen vacancy reduces two V<sup>5+</sup> to two V<sup>4+</sup> when there are no other dopants that affect the oxidation states of V. Therefore, the surface oxygen vacancy concentration can be reasonably estimated by quantifying the fraction of V that is present as V<sup>4+</sup>. From a previously reported study that used samples prepared in the same way as ours, <sup>27</sup> the percent concentration of V<sup>4+</sup> ( $\equiv$  %V<sup>4+</sup> = V<sup>4+</sup>/(V<sup>4+</sup> + V<sup>5+</sup>) × 100) of the epitaxially-grown single crystalline sample was determined to have a %V<sup>4+</sup> of 3.7%. This is equivalent to  $\sim$  0.6 at% (with respect to total number of atoms), meaning that the surface oxygen vacancy concentration of the epitaxially-grown single-crystalline sample is  $\sim$  0.3 at%. The measured

work function for undoped BiVO<sub>4</sub> with 0.3 at% oxygen vacancies (4.94 eV) is within the range between the calculated work function for the pristine (5.40 eV) and 1 at% oxygen vacancy concentration (4.86 eV). These comparisons demonstrate that our calculations are able to capture the change in the work function in the presence of oxygen vacancies. To our knowledge, this is one of the first direct comparisons between calculations and measurements on single-crystalline samples with well-defined surfaces and quantified composition (in stoichiometry or estimated %V<sup>4+</sup>).

#### 8 Discussion

We now discuss the different behaviors of the bulk and surface polarons that arise from the presence of oxygen vacancies in BiVO<sub>4</sub>. Based on an analysis of single-particle energies, Wiktor et al. <sup>36</sup> report that holes tend to localize at the *pristine* surface (i.e., without oxygen vacancies) and electron polarons tend to be stable in the pristine bulk, thus hinting at a robust charge separation mechanism. Our study of the defective surface with oxygen vacancies illustrates that the presence of oxygen vacancies leads to localization of electrons in various configurations, which may therefore promote charge recombination at the surface. For the (010) surface termination that favors electron accumulation, we find that these electrons form small polarons that tend to remain localized and immobile around the defect site. Using a combination of DFT+U and hybrid functional calculations, Hegner et al<sup>45</sup> proposed a picture similar to ours, where oxygen migration in the bulk faces moderate (0.2-0.4 eV) energy barriers and thus may lead to increased ionic and consequently electronic conductivity; in contrast, migration at the surface has large ( $\sim 1 \text{ eV}$ ) energy barriers to ionic (and consequently electronic) migration and are thus immobile. In addition to the neutral charge state considered in Ref. 45, we considered the 1+ and 2+ charge states of the oxygen vacancy. Furthermore, the ionic migration reported in Hegner et al is only part of the picture; that is, the energy barrier to polaron hopping (without any ionic migration) is small

enough in the bulk for polarons to contribute to mobility via polaron hopping but is less favorable for the surface polaron near an oxygen vacancy. Rossell et al.  $^{73}$  reported surface reduction of V sites using electron energy loss spectroscopy in combination with scanning transmission electron microscopy and interpreted this as segregation of oxygen vacancies at the surface, which is consistent with our observation of surface polarons accumulating in the presence of surface defects. Consistently, using differential absorption spectroscopy, Selim et al. suggested that the change in conductivity with moderate thermal heating arises from de-trapping oxygen vacancies.  $^{44}$  In fact they report the ionization energy of  $V^{4+}$  to  $V^{5+}$  to be  $\sim 0.2$  eV, in close agreement with bulk oxygen vacancy ionization energy reported in Ref. 21, further confirming that our methodology and the chosen level of theory are appropriate.

We note that our characterization of the surface oxygen vacancy is at 0 K and referenced to the vacuum. As with band alignments, we anticipate temperature corrections (and separately solvation effects) to play a critical role in the electronic behavior of these defects. Ref. 37 reported a reduction in electron polaron binding energies at finite temperature on the order of 200 meV for bulk polarons; a similar effect may occur for surface polarons. The pattern of surface relaxation at 0 K described in Section 5.1 also occurs at finite temperature,  $^{36}$  as this minimizes dangling bonds and is energetically favorable. Thus we would anticipate there would likewise be a tendency for electron accumulation at the surface. Another anticipated effect is temperature fluctuations in band edges, as in the case of WO<sub>3</sub>, which has on average fluctuations of 0.3 eV at 300 K.<sup>69</sup> BiVO<sub>4</sub> and WO<sub>3</sub> have comparable dielectric constants and longitudinal optical phonon frequencies (BiVO<sub>4</sub>:  $\varepsilon_{\infty} = 6.9$ ,  $^{14}$   $\omega_{LO} = 828$  cm<sup>-1</sup>;  $^{72.74}$  WO<sub>3</sub>:  $\varepsilon_{\infty} = 4.5$ ,  $^{69}$   $\omega_{LO} = 842$  cm<sup>-1</sup>  $^{75}$ ), and therefore comparable electron-phonon coupling strengths may be expected. Thus, we anticipate comparable band edge fluctuations at ambient conditions for BiVO<sub>4</sub>.

Ultimately, in addition to temperature, the interface with water will heavily determine the reactivity for water splitting for which surface defects will play an important role. When used without any oxygen evolution catalyst, BiVO<sub>4</sub> has relatively low photocurrent densities and its photocurrent onset is shifted towards the positive direction because its surface is not catalytic for water oxidation.  $^{76,77}$  The resulting surface accumulated holes can lead to surface recombination and/or photocorrosion.  $^{76}$  Whether the surface electron polaron plays an active, indirect, or passive role in charge transfer reactions and the overall reaction of water oxidation depends critically on the nature of the interface. Therefore, a further study is necessary to investigate how the surface oxygen vacancies and polaron formation are affected when the surface of BiVO<sub>4</sub> is in contact with water and with oxygen evolution catalysts in order to understand the overall photoelectrochemical properties of the this oxide system.

Overall, our findings suggest the following implications of oxygen vacancies to photoelectrochemical performance. First, surface polarons derived from oxygen vacancies are expected to contribute little to the overall mobility of electrons in BiVO<sub>4</sub> as a photoanode. Second, such electron polarons may act as recombination centers for holes shuttled towards the (010) surface during water oxidation if the interfacial hole transfer for oxygen evolution is slow. Third, the tendency to form small polarons at the surface will have a large impact on the interaction of the BiVO<sub>4</sub> surface with the oxygen evolution catalyst and interfacial water, and may significantly affect the interfacial charge transfer and/or recombination. Thus, it is critical when comparing theory and experiment to have a thorough characterization of surface defects. We expect water adsorption, surface terminations, and the addition of the oxygen evolution catalyst to heavily interact with surface defects and play an important role in the overall performance of BiVO<sub>4</sub> as a photoanode. Work is in progress to construct a holistic understanding of interfacial properties of BiVO<sub>4</sub>.

#### 9 Conclusions

In conclusion, we presented a systematic study of the (010) surface in  $BiVO_4$  with and without oxygen vacancies using first-principles calculations and compared them with experimental measurements. First, we benchmarked DFT, DFT+U and hybrid functionals for the

bulk and pristine surface, comparing lattice parameters and band gaps, and showed hybrids are the minimum level of theory needed to describe the band alignment. We validated our structural model and level of theory for slab calculations; our calculated band alignment and work function show excellent agreement with measurements obtained from single-crystalline samples when thermal renormalization, exciton effects, and spin-orbit coupling are taken into account. With an accurate model of the pristine surface, we next investigate the influence of surface reconstructions. While the (1x1) surface reconstruction results in minimal in-plane structural relaxation, the out-of-plane relaxations lead to an alternating pattern of contracted and elongated Bi-O and V-O bonds within the first two layers of the surface. For the (010) surface, this pattern of relaxation leads to a potential well for which electron accumulation is expected.

Such an electron accumulation is closely related to the formation of oxygen vacancies and small polarons. Similar to the bulk, surface polarons may form at a pristine or substoichiometric surface. Although polaron configurations analogous to the bulk are stable at the surface, the difference in relative stabilities of various configurations is smaller (by around 0.15 eV) than in the bulk. We attribute this difference to the fact that polaron formation is accompanied by a local lattice expansion that competes with surface relaxations.

To explore the thermodynamic stability and charge transition levels (CTLs) of possible charge states for the oxygen vacancy, we calculated the defect formation energy diagram. For both the bulk and surface, the oxygen vacancy is found to be a deep donor. In contrast to the bulk oxygen vacancies, the surface polaron is a much deeper donor (relative to the conduction band minimum) and also energetically far from the surface or bulk polaron level of a pristine slab. This indicates that while bulk polarons may contribute to mobility, surface polarons likely do not.

Finally, we performed a study of the variation of the work function in BiVO<sub>4</sub> with oxygen vacancy concentration. We found good agreement between measured single-crystalline samples and calculated values for the defect-free, pristine structure. More importantly, we

showed that our calculations capture and quantify the change in work function in the presence of oxygen vacancies in epitaxially-grown single-crystalline samples. This consequently confirms the validity of our structural model and will allow for more meaningful comparison and conclusions when studying properties of polycrystalline BiVO<sub>4</sub> in photoelectrochemical devices.

Overall, our study showed that 1) hybrid functionals are needed to accurately capture band alignment, 2) while the role of oxygen vacancies at the surface may be beneficial in some aspects (e.g., adsorption), its tendency for charge localization may be harmful to conductivity and lead to recombination centers that consume holes needed for water oxidation, and 3) defects in the bulk and at the surface behave differently and their different behavior must be taken into account to understand the photoelectrochemical behavior of BiVO<sub>4</sub>. We expect surface oxygen vacancies to play a critical and diverse role in water splitting reactions, particularly in charge transfer mechanisms when coupled with the oxygen evolution catalyst and when interfaced with water. Our study lays the groundwork for understanding electronic behavior and polaron formation of surface oxygen vacancies in BiVO<sub>4</sub>, and overall for other catalytic metal oxides.

## Acknowledgements

The authors thank David Starr and Marco Favaro for fruitful discussions on single crystalline measurements. This material is based upon work supported by the National Science Foundation (NSF) under Grant No. CHE-1764399. Part of this research used resources of the Center for Functional Nanomaterials, which is a U.S. DOE Office of Science User Facility, at Brookhaven National Laboratory under Contract No. DE-SC0012704. P.S. and J.K. are supported by the Army Research Office (W911NF-17-1-0254) and NSF CAREER (DMR-1752797). This work was completed in part with resources provided by the University of Chicago's Research Computing Center.

## Supporting Information Available

The following files are available free of charge: bvo-surf-supplementary.pdf: procedure for photoemission spectroscopy measurements and work function determination, comparison of  $\tilde{V}$  with DDH, convergence of slab calculations, charge state corrections, determination of work function and Fermi level, pristine bulk and surface structural and electronic parameters, determination of chemical potential in defect formation energies

Input files, structure files, and scripts for generating the data in the main text and SI are available on QRESP (www.qresp.org), an open-source curation and exploration software for reproducibility in scientific research.

#### References

- (1) Nozik, A. J. Photoelectrochemistry: Applications to Solar Energy Conversion. <u>Annual</u> Review of Physical Chemistry **1978**, 29, 189–222.
- (2) Grätzel, M. Photoelectrochemical Cells. Nature **2001**, 414, 338–344.
- (3) Turner, J. A. Sustainable Hydrogen Production. Science 2004, 305, 972–974.
- (4) Walter, M. G.; Warren, E. L.; McKone, J. R.; Boettcher, S. W.; Mi, Q.; Santori, E. A.; Lewis, N. S. Solar Water Splitting Cells. Chemical Reviews **2010**, 110, 6446–6473.
- (5) McKone, J. R.; Lewis, N. S.; Gray, H. B. Will Solar-Driven Water-Splitting Devices See the Light of Day? Chemistry of Materials **2014**, 26, 407–414.
- (6) Lewis, N. S. Introduction: Solar Energy Conversion. <u>Chemical Reviews</u> **2015**, <u>115</u>, 12631–12632.
- (7) Chu, S.; Li, W.; Yan, Y.; Hamann, T.; Shih, I.; Wang, D.; Mi, Z. Roadmap on Solar Water Splitting: Current Status and Future Prospects. Nano Futures **2017**, 1, 022001.

- (8) Zhu, S.; Wang, D. Photocatalysis: Basic Principles, Diverse Forms of Implementations and Emerging Scientific Opportunities. Advanced Energy Materials **2017**, 7, 1700841.
- (9) Park, Y.; McDonald, K. J.; Choi, K.-S. Progress in Bismuth Vanadate Photoanodes for Use in Solar Water Oxidation. Chem. Soc. Rev. **2013**, 42, 2321–2337.
- (10) Kim, T. W.; Choi, K.-S. Nanoporous BiVO<sub>4</sub> Photoanodes with Dual-Layer Oxygen Evolution Catalysts for Solar Water Splitting. <u>Science</u> **2014**, <u>343</u>, 990–994.
- (11) Favaro, M.; Uecker, R.; Nappini, S.; Píš, I.; Magnano, E.; Bluhm, H.; van de Krol, R.; Starr, D. E. Chemical, Structural, and Electronic Characterization of the (010) Surface of Single Crystalline Bismuth Vanadate. <u>The Journal of Physical Chemistry C</u> 2019, 123, 8347–8359.
- (12) Cooper, J. K.; Gul, S.; Toma, F. M.; Chen, L.; Glans, P.-A.; Guo, J.; Ager, J. W.; Yano, J.; Sharp, I. D. Electronic Structure of Monoclinic BiVO<sub>4</sub>. Chemistry of Materials **2014**, 26, 5365–5373.
- (13) Kudo, A.; Omori, K.; Kato, H. A Novel Aqueous Process for Preparation of Crystal Form-Controlled and Highly Crystalline BiVO<sub>4</sub> Powder from Layered Vanadates at Room Temperature and Its Photocatalytic and Photophysical Properties. <u>Journal of the American Chemical Society</u> **1999**, 121, 11459–11467.
- (14) Kim, T. W.; Ping, Y.; Galli, G. A.; Choi, K.-S. Simultaneous Enhancements in Photon Absorption and Charge Transport of Bismuth Vanadate Photoanodes for Solar Water Splitting. <u>Nature Communications</u> 2015, 6, 8769.
- (15) Malashchonak, M. V.; Streltsov, E. A.; Kuliomin, D. A.; Kulak, A. I.; Mazanik, A. V. Monoclinic Bismuth Vanadate Band Gap Determination by Photoelectrochemical Spectroscopy. Materials Chemistry and Physics 2017, 201, 189–193.

- (16) Payne, D. J.; Robinson, M. D. M.; Egdell, R. G.; Walsh, A.; McNulty, J.; Smith, K. E.; Piper, L. F. J. The Nature of Electron Lone Pairs in BiVO<sub>4</sub>. <u>Applied Physics Letters</u> 2011, 98, 212110.
- (17) Murphy, A.; Barnes, P.; Randeniya, L.; Plumb, I.; Grey, I.; Horne, M.; Glasscock, J. Efficiency of Solar Water Splitting Using Semiconductor Electrodes. <u>International Journal</u> of Hydrogen Energy **2006**, 31, 1999–2017.
- (18) Kim, J. H.; Jang, J.-W.; Jo, Y. H.; Abdi, F. F.; Lee, Y. H.; van de Krol, R.; Lee, J. S. Hetero-Type Dual Photoanodes for Unbiased Solar Water Splitting with Extended Light Harvesting. <u>Nature Communications</u> 2016, 7, 13380.
- (19) Tolod, K. R.; Hernández, S.; Russo, N.; Tolod, K. R.; Hernández, S.; Russo, N. Recent Advances in the BiVO<sub>4</sub> Photocatalyst for Sun-Driven Water Oxidation: Top-Performing Photoanodes and Scale-Up Challenges. Catalysts 2017, 7, 13.
- (20) Cooper, J. K.; Scott, S. B.; Ling, Y.; Yang, J.; Hao, S.; Li, Y.; Toma, F. M.; Stutzmann, M.; Lakshmi, K. V.; Sharp, I. D. Role of Hydrogen in Defining the N-Type Character of BiVO<sub>4</sub> Photoanodes. Chemistry of Materials 2016, 28, 5761–5771.
- (21) Seo, H.; Ping, Y.; Galli, G. Role of Point Defects in Enhancing Conductivity of BiVO<sub>4</sub>. Chemistry of Materials **2018**, 30, 7793–7802.
- (22) Zhao, X.; Hu, J.; Yao, X.; Chen, S.; Chen, Z. Clarifying the Roles of Oxygen Vacancy in W-Doped BiVO<sub>4</sub> for Solar Water Splitting. <u>ACS Applied Energy Materials</u> **2018**, <u>1</u>, 3410–3419.
- (23) Zhao, Z.; Luo, W.; Li, Z.; Zou, Z. Density Functional Theory Study of Doping Effects in Monoclinic Clinobisvanite BiVO4. Physics Letters A **2010**, 374, 4919–4927.
- (24) Zhang, J.; Deng, M.; Ren, F.; Wu, Y.; Wang, Y. Effects of Mo/W Codoping on the

- Visible-Light Photocatalytic Activity of Monoclinic BiVO<sub>4</sub> within the GGA+U Framework. RSC Advances **2016**, 6, 12290–12297.
- (25) Rettie, A. J. E.; Lee, H. C.; Marshall, L. G.; Lin, J.-F.; Capan, C.; Lindemuth, J.; Mc-Cloy, J. S.; Zhou, J.; Bard, A. J.; Mullins, C. B. Combined Charge Carrier Transport and Photoelectrochemical Characterization of BiVO<sub>4</sub> Single Crystals: Intrinsic Behavior of a Complex Metal Oxide. <u>Journal of the American Chemical Society</u> 2013, <u>135</u>, 11389–11396.
- (26) Kweon, K. E.; Hwang, G. S.; Kim, J.; Kim, S.; Kim, S. Electron Small Polarons and Their Transport in Bismuth Vanadate: A First Principles Study. <u>Physical Chemistry</u> Chemical Physics **2015**, 17, 256–260.
- (27) Zhang, W.; Wu, F.; Li, J.; Yan, D.; Tao, J.; Ping, Y.; Liu, M. Unconventional Relation between Charge Transport and Photocurrent via Boosting Small Polaron Hopping for Photoelectrochemical Water Splitting. <u>ACS Energy Letters</u> **2018**, 3, 2232–2239.
- (28) Zhang, W.; Yan, D.; Li, J.; Wu, Q.; Cen, J.; Zhang, L.; Orlov, A.; Xin, H.; Tao, J.; Liu, M. Anomalous Conductivity Tailored by Domain-Boundary Transport in Crystalline Bismuth Vanadate Photoanodes. Chemistry of Materials **2018**, 30, 1677–1685.
- (29) Qiu, W.; Xiao, S.; Ke, J.; Wang, Z.; Tang, S.; Zhang, K.; Qian, W.; Huang, Y.; Huang, D.; Tong, Y.; Yang, S. Freeing the Polarons to Facilitate Charge Transport in BiVO4 from Oxygen Vacancies with an Oxidative 2D Precursor. <u>Angewandte Chemie International Edition</u> **2019**, DOI: 10.1002/anie.201912475.
- (30) Zhang, W.; Song, L.; Cen, J.; Liu, M. Mechanistic Insights into Defect-Assisted Carrier Transport in Bismuth Vanadate Photoanodes. <u>The Journal of Physical Chemistry C</u> **2019**, 123, 20730–20736.
- (31) Walsh, A.; Yan, Y.; Huda, M. N.; Al-Jassim, M. M.; Wei, S.-H. Band Edge Electronic

- Structure of BiVO <sub>4</sub>: Elucidating the Role of the Bi s and V d Orbitals. <u>Chemistry of Materials</u> **2009**, 21, 547–551.
- (32) Zhao, Z.; Li, Z.; Zou, Z. Electronic Structure and Optical Properties of Monoclinic Clinobisvanite BiVO<sub>4</sub>. Physical Chemistry Chemical Physics **2011**, 13, 4746–4753.
- (33) Ding, K.; Chen, B.; Li, Y.; Zhang, Y.; Chen, Z. Comparative Density Functional Theory Study on the Electronic and Optical Properties of BiMO4 (M = V, Nb, Ta). <u>Journal</u> of Materials Chemistry A **2014**, 2, 8294.
- (34) Wiktor, J.; Reshetnyak, I.; Ambrosio, F.; Pasquarello, A. Comprehensive Modeling of the Band Gap and Absorption Spectrum of BiVO<sub>4</sub>. Physical Review Materials **2017**, 1.
- (35) Wu, F.; Ping, Y. Combining Landau–Zener Theory and Kinetic Monte Carlo Sampling for Small Polaron Mobility of Doped BiVO <sub>4</sub> from First-Principles. <u>Journal of Materials</u> Chemistry A **2018**, 6, 20025–20036.
- (36) Wiktor, J.; Pasquarello, A. Electron and Hole Polarons at the BiVO<sub>4</sub> –Water Interface. ACS Applied Materials & Interfaces **2019**, 11, 18423–18426.
- (37) Wiktor, J.; Ambrosio, F.; Pasquarello, A. Role of Polarons in Water Splitting: The Case of BiVO<sub>4</sub>. ACS Energy Letters **2018**, 3, 1693–1697.
- (38) Wang, G.; Ling, Y.; Lu, X.; Qian, F.; Tong, Y.; Zhang, J. Z.; Lordi, V.; Rocha Leao, C.; Li, Y. Computational and Photoelectrochemical Study of Hydrogenated Bismuth Vanadate. The Journal of Physical Chemistry C 2013, 117, 10957–10964.
- (39) Yin, W.-J.; Wei, S.-H.; Al-Jassim, M. M.; Turner, J.; Yan, Y. Doping Properties of Monoclinic BiVO 4 Studied by First-Principles Density-Functional Theory. <u>Physical</u> Review B 2011, 83, 115102.

- (40) Wang, D.; Jiang, H.; Zong, X.; Xu, Q.; Ma, Y.; Li, G.; Li, C. Crystal Facet Dependence of Water Oxidation on BiVO<sub>4</sub> Sheets under Visible Light Irradiation. <u>Chemistry A</u> European Journal **2011**, 17, 1275–1282.
- (41) Hu, J.; Chen, W.; Zhao, X.; Su, H.; Chen, Z. Anisotropic Electronic Characteristics, Adsorption, and Stability of Low-Index BiVO<sub>4</sub> Surfaces for Photoelectrochemical Applications. ACS Applied Materials & Interfaces 2018, 10, 5475–5484.
- (42) Li, R.; Zhang, F.; Wang, D.; Yang, J.; Li, M.; Zhu, J.; Zhou, X.; Han, H.; Li, C. Spatial Separation of Photogenerated Electrons and Holes among {010} and {110} Crystal Facets of BiVO<sub>4</sub>. Nature Communications **2013**, 4, 1432.
- (43) Hu, J.; Zhao, X.; Chen, W.; Su, H.; Chen, Z. Theoretical Insight into the Mechanism of Photoelectrochemical Oxygen Evolution Reaction on BiVO<sub>4</sub> Anode with Oxygen Vacancy. The Journal of Physical Chemistry C **2017**, 121, 18702–18709.
- (44) Selim, S.; Pastor, E.; García-Tecedor, M.; Morris, M. R.; Francas, L.; Sachs, M.; Moss, B.; Corby, S.; Mesa, C. A.; Gimenez, S.; Kafizas, A.; Bakulin, A. A.; Durrant, J. R. Impact of Oxygen Vacancy Occupancy on Charge Carrier Dynamics in BiVO<sub>4</sub> Photoanodes. <u>Journal of the American Chemical Society</u> **2019**, DOI: 10.1021/jacs.9b09056.
- (45) Hegner, F. S.; Forrer, D.; Galán-Mascarós, J. R.; López, N.; Selloni, A. Versatile Nature of Oxygen Vacancies in Bismuth Vanadate Bulk and (001) Surface. <u>The Journal of Physical Chemistry Letters</u> **2019**, <u>10</u>, 6672–6678.
- (46) Yang, J.; Wang, D.; Zhou, X.; Li, C. A Theoretical Study on the Mechanism of Photocatalytic Oxygen Evolution on BiVO<sub>4</sub> in Aqueous Solution. <u>Chemistry A European Journal</u> **2013**, 19, 1320–1326.
- (47) Oshikiri, M.; Boero, M. Water Molecule Adsorption Properties on the BiVO<sub>4</sub> (100) Surface. The Journal of Physical Chemistry B **2006**, 110, 9188–9194.

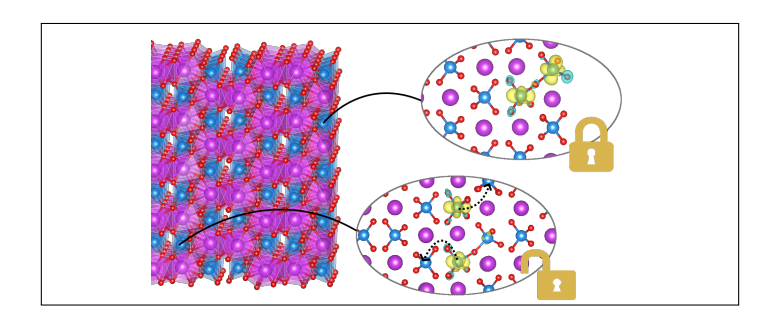
- (48) Crespo-Otero, R.; Walsh, A. Variation in Surface Ionization Potentials of Pristine and Hydrated BiVO<sub>4</sub>. The Journal of Physical Chemistry Letters **2015**, 6, 2379–2383.
- (49) Ambrosio, F.; Wiktor, J.; Pasquarello, A. pH-Dependent Surface Chemistry from First Principles: Application to the BiVO<sub>4</sub> (010)–Water Interface. <u>ACS Applied Materials & Interfaces</u> **2018**, 10, 10011–10021.
- (50) Hohenberg, P.; Kohn, W. Inhomogeneous Electron Gas. <u>Physical Review</u> **1964**, <u>136</u>, B864–B871.
- (51) Kohn, W.; Sham, L. J. Self-Consistent Equations Including Exchange and Correlation Effects. Physical Review **1965**, 140, A1133–A1138.
- (52) Schlipf, M.; Gygi, F. Optimization Algorithm for the Generation of ONCV Pseudopotentials. Computer Physics Communications **2015**, 196, 36–44.
- (53) Hamann, D. R. Optimized Norm-Conserving Vanderbilt Pseudopotentials. <u>Physical</u> Review B **2013**, 88, 085117.
- (54) Giannozzi, P. et al. QUANTUM ESPRESSO: A Modular and Open-Source Software Project for Quantum Simulations of Materials. <u>Journal of Physics: Condensed Matter</u> **2009**, 21, 395502.
- (55) Giannozzi, P. et al. Advanced Capabilities for Materials Modelling with Quantum ESPRESSO. Journal of Physics: Condensed Matter **2017**, 29, 465901.
- (56) Dudarev, S. L.; Botton, G. A.; Savrasov, S. Y.; Humphreys, C. J.; Sutton, A. P. Electron-Energy-Loss Spectra and the Structural Stability of Nickel Oxide: An LSDA+U Study. Physical Review B 1998, 57, 1505–1509.
- (57) Solovyev, I. V.; Dederichs, P. H.; Anisimov, V. I. Corrected Atomic Limit in the Local-Density Approximation and the Electronic Structure of <u>d</u> Impurities in Rb. <u>Physical Review B</u> **1994**, 50, 16861–16871.

- (58) Skone, J. H.; Govoni, M.; Galli, G. Self-Consistent Hybrid Functional for Condensed Systems. Physical Review B **2014**, 89, 195112.
- (59) Sun, W.; Ceder, G. Efficient Creation and Convergence of Surface Slabs. <u>Surface Science</u> **2013**, 617, 53–59.
- (60) Freysoldt, C.; Grabowski, B.; Hickel, T.; Neugebauer, J.; Kresse, G.; Janotti, A.; Van de Walle, C. G. First-Principles Calculations for Point Defects in Solids. <u>Reviews of Modern Physics</u> 2014, 86, 253–305.
- (61) Freysoldt, C.; Neugebauer, J. First-Principles Calculations for Charged Defects at Surfaces, Interfaces, and Two-Dimensional Materials in the Presence of Electric Fields. Physical Review B 2018, 97, 205425.
- (62) Cooper, J. K.; Gul, S.; Toma, F. M.; Chen, L.; Liu, Y.-S.; Guo, J.; Ager, J. W.; Yano, J.; Sharp, I. D. Indirect Bandgap and Optical Properties of Monoclinic Bismuth Vanadate. The Journal of Physical Chemistry C 2015, 119, 2969–2974.
- (63) Kweon, K. E.; Hwang, G. S. Hybrid Density Functional Study of the Structural, Bonding, and Electronic Properties of Bismuth Vanadate. <u>Physical Review B</u> 2012, <u>86</u>, 165209.
- (64) Payne, D. J.; Egdell, R. G.; Walsh, A.; Watson, G. W.; Guo, J.; Glans, P.-A.; Learmonth, T.; Smith, K. E. Electronic Origins of Structural Distortions in Post-Transition Metal Oxides: Experimental and Theoretical Evidence for a Revision of the Lone Pair Model. Physical Review Letters 2006, 96, 157403.
- (65) Zhao, Z.; Li, Z.; Zou, Z. Structure and Energetics of Low-Index Stoichiometric Monoclinic Clinobisvanite BiVO<sub>4</sub> Surfaces. RSC Advances **2011**, 1, 874–883.
- (66) Tachikawa, T.; Ochi, T.; Kobori, Y. Crystal-Face-Dependent Charge Dynamics on

- a BiVO<sub>4</sub> Photocatalyst Revealed by Single-Particle Spectroelectrochemistry.  $\underline{ACS}$  Catalysis **2016**, 6, 2250–2256.
- (67) Li, D.; Liu, Y.; Shi, W.; Shao, C.; Wang, S.; Ding, C.; Liu, T.; Fan, F.; Shi, J.; Li, C. Crystallographic-Orientation-Dependent Charge Separation of BiVO<sub>4</sub> for Solar Water Oxidation. ACS Energy Letters 2019, 4, 825–831.
- (68) Smondyrev, M. A. Diagrams in the Polaron Model. <u>Theoretical and Mathematical</u> Physics **1986**, 68, 653–664.
- (69) Gerosa, M.; Gygi, F.; Govoni, M.; Galli, G. The Role of Defects and Excess Surface Charges at Finite Temperature for Optimizing Oxide Photoabsorbers. <u>Nature Materials</u> **2018**, 17, 1122–1127.
- (70) Park, H. S.; Kweon, K. E.; Ye, H.; Paek, E.; Hwang, G. S.; Bard, A. J. Factors in the Metal Doping of BiVO<sub>4</sub> for Improved Photoelectrocatalytic Activity as Studied by Scanning Electrochemical Microscopy and First-Principles Density-Functional Calculation. The Journal of Physical Chemistry C **2011**, 115, 17870–17879.
- (71) Hermans, Y.; Murcia-López, S.; Klein, A.; van de Krol, R.; Andreu, T.; Morante, J. R.; Toupance, T.; Jaegermann, W. Analysis of the Interfacial Characteristics of BiVO<sub>4</sub>/Metal Oxide Heterostructures and Its Implication on Their Junction Properties. Physical Chemistry Chemical Physics 2019, 21, 5086–5096.
- (72) Hermans, Y.; Klein, A.; Ellmer, K.; van de Krol, R.; Toupance, T.; Jaegermann, W. Energy-Band Alignment of BiVO<sub>4</sub> from Photoelectron Spectroscopy of Solid-State Interfaces. The Journal of Physical Chemistry C **2018**, 122, 20861–20870.
- (73) Rossell, M. D.; Agrawal, P.; Borgschulte, A.; Hébert, C.; Passerone, D.; Erni, R. Direct Evidence of Surface Reduction in Monoclinic BiVO<sub>4</sub>. Chemistry of Materials **2015**, <u>27</u>, 3593–3600.

- (74) Galembeck, A.; Alves, O. L. BiVO<sub>4</sub> Thin Film Preparation by Metalorganic Decomposition. Thin Solid Films **2000**, 365, 90–93.
- (75) Hamdi, H.; Salje, E. K. H.; Ghosez, P.; Bousquet, E. First-Principles Reinvestigation of Bulk WO<sub>3</sub>. Physical Review B **2016**, 94, 245124.
- (76) Seabold, J. A.; Choi, K.-S. Efficient and Stable Photo-Oxidation of Water by a Bismuth Vanadate Photoanode Coupled with an Iron Oxyhydroxide Oxygen Evolution Catalyst. Journal of the American Chemical Society **2012**, 134, 2186–2192.
- (77) Lee, D. K.; Choi, K.-S. Enhancing Long-Term Photostability of BiVO<sub>4</sub> Photoanodes for Solar Water Splitting by Tuning Electrolyte Composition. <u>Nature Energy</u> **2018**, <u>3</u>, 53–60.

# Graphical TOC Entry



# Supporting Information for The role of surface oxygen vacancies in $BiVO_4$

Wennie Wang,† Patrick James Strohbeen,‡ Dongho Lee,¶ Chenyu Zhou,§,∥ Jason Ken Kawasaki,‡ Kyoung-Shin Choi,¶ Mingzhao Liu,§ and Giulia Galli\*,†,⊥,#

†Pritzker School of Molecular Engineering, University of Chicago, Chicago, IL 60637, USA ‡Materials Science and Engineering, University of Wisconsin-Madison, Madison, WI 53706, USA

¶Department of Chemistry, University of Wisconsin-Madison, Madison, WI 53706, USA §Center for Functional Nanomaterials, Brookhaven National Laboratory, Upton, NY 11973, USA

|| Department of Materials Science and Chemical Engineering, Stony Brook University,
Stony Brook, NY 11794

⊥Materials Science Division and Center for Molecular Engineering, Argonne National

Laboratory, Lemont, Illinois 60439, USA

 $\#Department\ of\ Chemistry,\ University\ of\ Chicago,\ Chicago,\ IL\ 60615,\ USA$ 

E-mail: gagalli@uchicago.edu

# Experiment

#### Photoemission spectroscopy measurements

Room temperature ultra-violet photoemission (UPS) studies were conducted using a Thermofisher non-monochromatic He lamp with a main emission line of 21.2 eV (He  $1\alpha$ ) and an Omicron EA125 electron analyzer. We use a pass energy of 10 eV and an entrance and exit slit size of 1 mm, corresponding to a system resolution of 120 meV, as obtained from fitting a Gaussian broadened Fermi-Dirac distribution to a reference Fermi level measurement of an in-situ evaporated gold film.

The base pressure of the UPS chamber is  $1 \times 10^{-10}$  Torr and rises during lamp operation to roughly  $2 \times 10^{-8}$  Torr. The sample was indium bonded to a Mo sample plate and the film surface was contacted to the plate with Leitsilber 200 silver paint (Ted Pella Inc.). To remove as much of the solvent impurities before loading into the system, the silver paint was left to cure on the bench for an hour at  $100^{\circ}$ C, then outgassed in high vacuum ( $\sim 10^{-7}$  Torr) at  $150^{\circ}$ C for another hour. Once loaded into the measurement chamber the sample was further outgassed under UHV at  $175^{\circ}$ C for an hour. To check cleanliness, core levels were measured using X-ray photoemission spectroscopy (XPS) using non-monochromatic Mg K $\alpha$  emission at 1253.6 eV. The sample exhibited a weak C 1s peak in XPS (see Figure S1) from contamination that was unchanging as a function of additional outgas time and anneal temperature. Comparing intensities of the C 1s core level to the Bi 4f core level, we see an integrated intensity ratio of roughly 14.2:1 for Bi 4f:C 1s.

#### Work function measurement

In a photoemission measurement, the work function  $(\varphi)$  is determined from the low kinetic energy onset of the photoemission intensity. However, since there is a contact potential between the sample and the analyzer, the measured onset could be due to the sample work function  $\varphi_s$  or due to the analyzer work function  $\varphi_a$  (Figure S2a,b). In order to distinguish

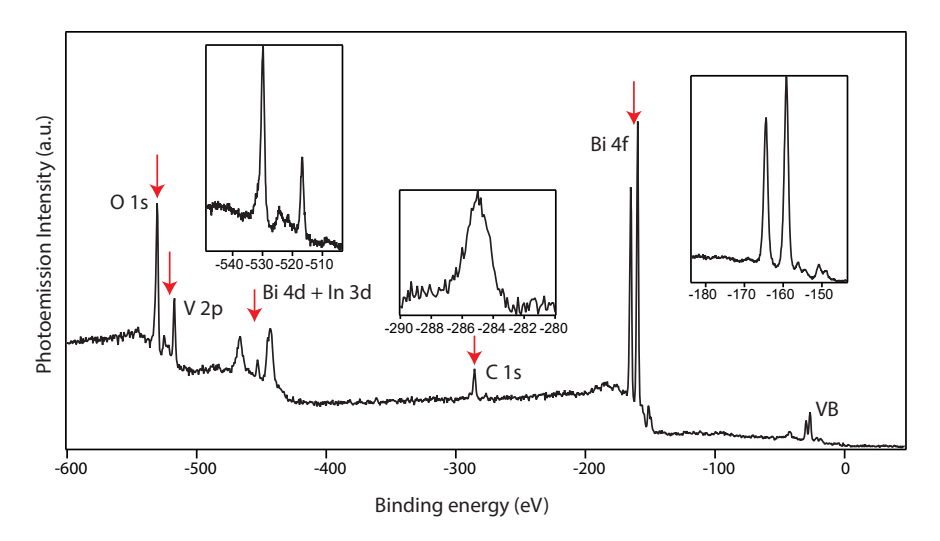


Figure S1: Mg  $\alpha$  XPS spectrum for the BiVO<sub>4</sub> sample. Insets are zoomed in scans of the V 2p, O 1s, Bi 4f, and C 1s core levels; we also observe Bi 4d core levels. We attribute the observation of indium 3d core levels to trace indium on the sample plate (used for bonding) or from the underlying ITO layer due to pinholes in the film.

the two work functions, measurements were performed as a function of increasing negative bias, which lifts the sample potential with respect to the analyzer potential and reveals the onset due to the sample (Figure S2c). By simple energy conservation, <sup>1</sup> the sample work function is given by:

$$\varphi_s = \lim_{V_{ext} < |\varphi_s - \varphi_a|} [h\nu - (E_{\text{kin,Fermi}} - E_{\text{kin,onset}})]$$
 (1)

,

whose limit is the constant value  $\varphi_s$  for negative sample biases when the vacuum potential of the sample is lifted above that of the analyzer (Figure S2c). Here,  $E_{\rm kin,onset}$  and  $E_{\rm kin,Fermi}$  are the low kinetic energy onset and the Fermi edge, respectively, as a function of applied external bias, and  $h\nu$  is the incident photon energy. For our EA125 analyzer, under typical measurement conditions with 10 eV pass energy,  $\varphi_a$  is approximately 4.5 eV, as determined by the relation  $h\nu = E_{\rm kin,Fermi} + \varphi_a$  (Figure S2).

 $E_{\text{kin,onset}}$  was determined by a linear extrapolation of the low kinetic energy onset of photoemission intensity measured on the sample.  $E_{\text{kin,Fermi}}$  was obtained from measurements

of the Fermi level on a spot welded Ta foil that is in electrical contact with the sample. An example of the extraction for both  $E_{\rm kin,onset}$  and  $E_{\rm kin,Fermi}$  is shown in Figure S3. As a result of the C contamination, some samples displayed multiple onset energies due to patchy contaminant coverage as discussed in Helander et. al. In these cases, the highest energy onset was the value taken to be the true sample onset energy. The extracted values of  $E_{\rm kin,Fermi}$ ,  $E_{\rm kin,onset}$ , and  $\varphi_s$  for the BiVO<sub>4</sub> sample is shown in Figure S4.

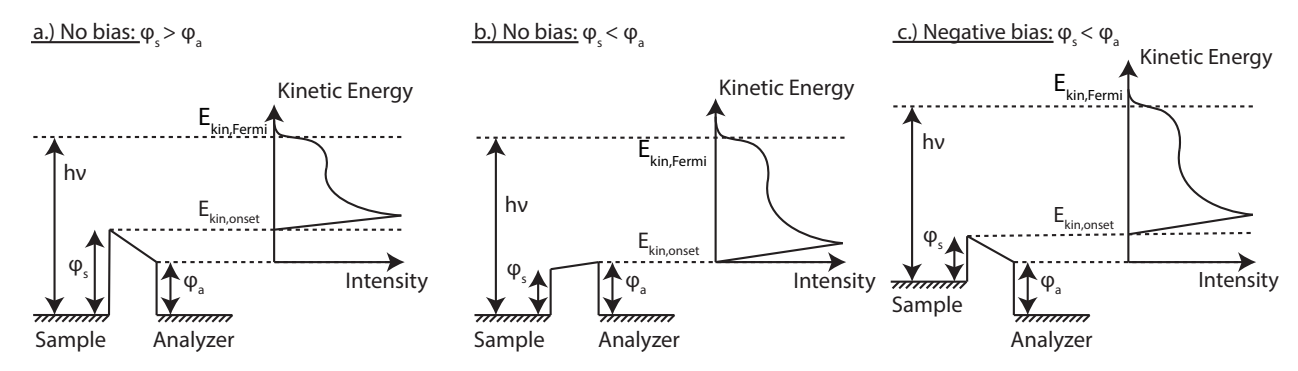


Figure S2: Schematic drawings of band alignments and shifts as a function of bias where  $\varphi_s$ ,  $\varphi_a$ , and  $h\nu$  are the sample work function, analyzer work function, and photon energy, respectively. The zero of kinetic energy is given by the vacuum energy at the analyzer, which yields the familiar relation  $h\nu = E_{\rm kin,Fermi} + \varphi_a$ . (a) If  $\varphi_s > \varphi_a$ , then the low kinetic energy onset for the spectrum  $E_{\rm kin,onset}$  results from photoexcitation above the sample work function. (b) However, if  $\varphi_s < \varphi_a$  then the  $E_{\rm kin,onset}$  is determined by the analyzer work function. (c) With sufficient negative biasing on the sample, the  $E_{\rm kin,onset}$  is due to the sample work function.

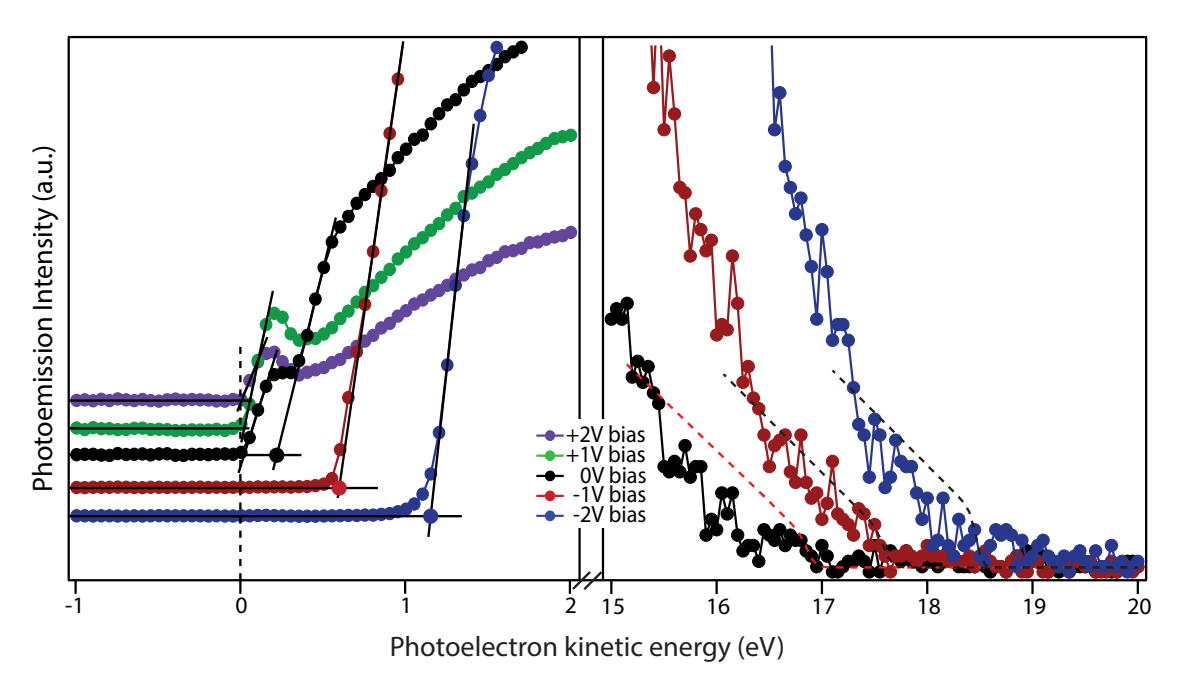


Figure S3: Raw spectra for the  $BiVO_4$  sample showing the band shifts and extraction of (left)  $E_{\rm kin,onset}$  and (right)  $E_{\rm kin,Fermi}$  energies as a function of sample bias. The low kinetic energy data (left) are measured on the  $BiVO_4$  sample, where the vertical dotted line shows the analyzer work function. The high kinetic energy data are measured on a Ta foil, which is in electrical contact with the sample.

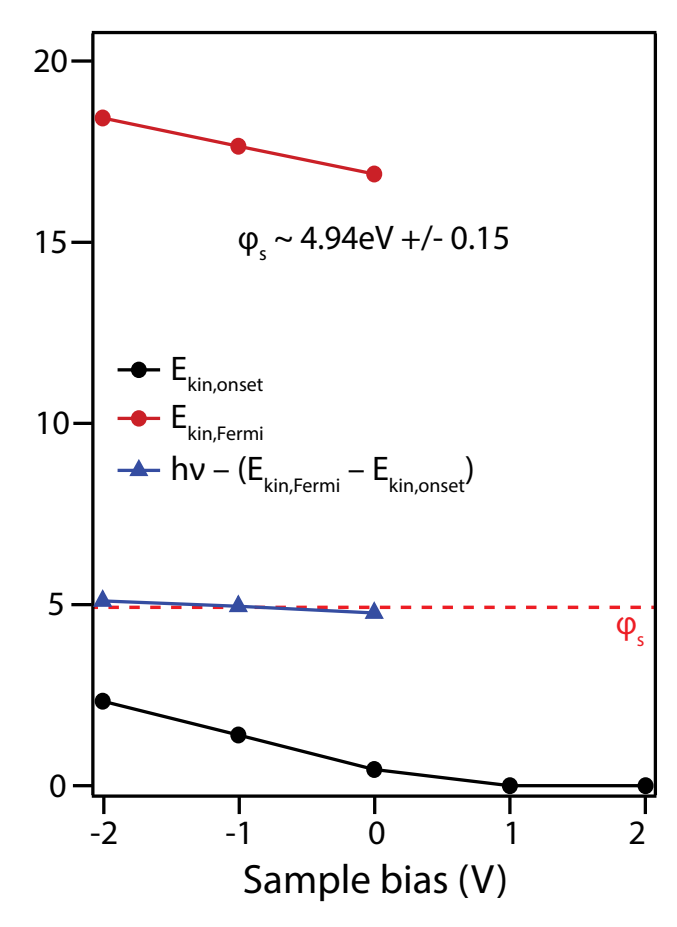


Figure S4: Extracted values of  $E_{\rm kin,Fermi}$ ,  $E_{\rm kin,onset}$ , and  $[h\nu - (E_{\rm kin,Fermi} - E_{\rm kin,onset})]$  for the BiVO<sub>4</sub> sample. The red dashed line represents the asymptotic value that is taken to be  $\varphi_s$ . Reported error is the broadening observed in the zero bias Fermi-Dirac fit.

# Computational

Input files, structure files, and scripts for generating the data in the main text and SI are available on QRESP (www.qresp.org), an open-source curation and exploration software for reproducibility in scientific research.

# Comparison of $\widetilde{V}$ with DDH

A comparison of the bulk lattice parameters, band gap, work function, and band alignment may be found in Tables S3 and S4. In Figure S5 the average electrostatic potential at the DDH level is shown. Similar to DFT+U, we find that a potential well near the surface forms at the surface when using DDH functionals. The main difference between results obtained at DFT+U and DDH levels of theory is the variation in  $\tilde{V}$  peaks between layers, which correspond to alternating planes of Bi/V and O. In DFT+U, the  $\tilde{V}$  variation between Bi/V and O planes is smaller. This is consistent with the the general observation that the inclusion of Hartree-Fock (HF) exact exchange leads to a greater localization of charge; specifically for BiVO<sub>4</sub>, increasing HF exchange leads to an increase of charge on O anions and charge depletion on Bi and V cations.<sup>2</sup> Nevertheless, we expect many of the conclusions on trends drawn using DFT+U to hold at the DDH level of theory.

## Convergence of slab calculations

We present the convergence of computed work functions and band alignments in with respect to chosen vacuum in the slab and number of atomic layers at the level of DFT+U in Table S1.

## Charge state corrections

The charge state correction is calculated following Freysoldt et al.<sup>3</sup> for 2D systems. We use for the static dielectric constant  $\varepsilon_0 = 52$ .<sup>4</sup> In our symmetric slabs, we manually shift the charges symmetrically, restrict the isolated range to one side, and double the isolated

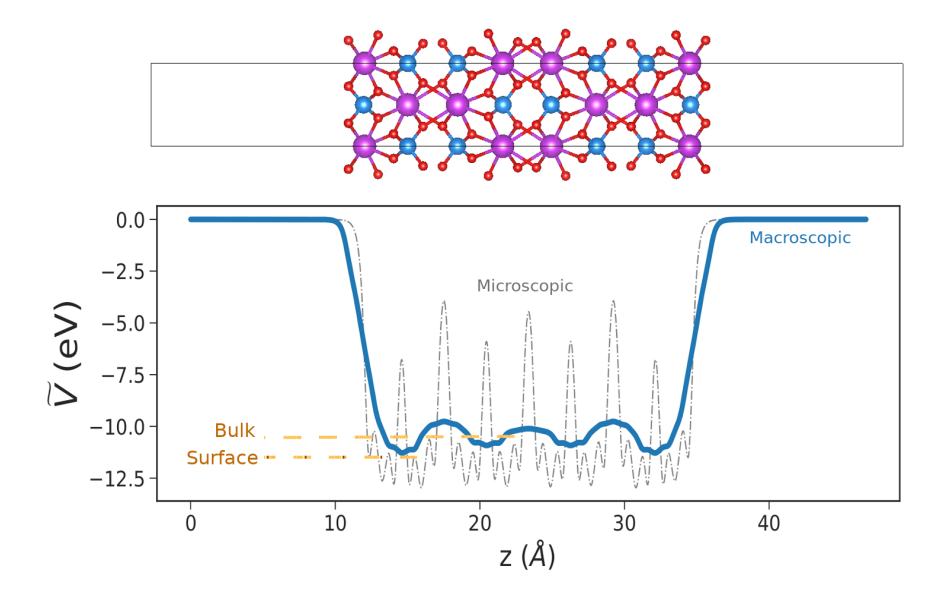


Figure S5: Microscopic and macroscopic average electrostatic potential  $\widetilde{V}$  of the (010) slab using DDH. The orange dashed lines indicate the average potential along z at the surface and that in the bulk.

Table S1: Convergence of work function  $\varphi$  and valence (VBM) and conduction (CBM) band edge positions with respect to vacuum and slab thickness for slab calculations obtained using DFT+U.

# layers	Vacuum	Surf. E	$\varphi$	CBM	VBM
	(Å)	$(\mathrm{J/m^2})$	(eV)	(eV)	(eV)
8	10	0.324	5.368	5.003	7.343
8	15	0.324	5.452	5.017	7.366
8	20	0.324	5.452	5.017	7.367
12	20	0.325	5.401	5.050	7.303
20	20	0.337	5.374	5.047	7.319

energy before subtracting the periodic energy for final the charge state correction. With an exposed surface there is less screening, and the charge state correction can be large (on the order of eVs) compared to those of their bulk counterparts. For example, the charge state correction of a 1+ oxygen vacancy on the BiVO<sub>4</sub> (010) surface is approximately a -0.88 eV correction, which is comparable to the corrections found for the Si surface;<sup>3</sup> in the bulk,<sup>5</sup> it is approximately 0.027 eV. We found a vacuum thickness of 25 Å to be sufficient, with changes in the formation energy to be 0.05 eV with larger vacuum sizes. Slab thicknesses up to 12 layers were tested, with the surface polaron hopping barrier (see the main text for

discussion) varying by  $\approx 0.06 \text{ eV}$ .

#### Determination of work function and Fermi level

The determination of the work function is based on the identification of the Fermi level from a density states calculation using the formula:

$$N = \int d\varepsilon \, g(\varepsilon) \cdot f(\varepsilon), \tag{2}$$

where N is the number of electrons,  $g(\varepsilon)$  is the density of states and  $f(\varepsilon)$  is the Fermi-Dirac distribution function. We target the intrinsic doping concentration  $n = N/\Omega = 0$  to extract an intrinsic Fermi level. In order to calculate the density of states to a high degree of accuracy, we use Wannier functions<sup>6</sup> to sample the bulk Brillouin Zone efficiently with  $100 \times 100 \times 100$  grids. Table S2 shows the relative positions of our calculated Fermi level at different levels of theory, which compares well with the measured Fermi level on single-crystalline samples ( $E_F = E_{\text{CBM}} - 0.3 \text{ eV}$ ).

The work function may be computed with two equivalent methods. The first method involves determining the work function directly from a the slab calculation.

$$\varphi_1 = V^{\text{vac}} - E_F^{\text{slab}},\tag{3}$$

where  $V^{\text{vac}}$  is the vacuum potential and  $E_F^{\text{slab}}$  is the Fermi level of the slab. The second method references the work function to the Fermi level in a bulk calculation.

$$\varphi_2 = V^{\text{vac}} - [E_F^{\text{bulk}} - (\tilde{V}^{\text{bulk}} - \tilde{V}^{\text{slab}})], \tag{4}$$

where  $\tilde{V}$  indicates the average electrostatic potential. Indeed, we found that the two methods yield results that differ by  $\sim 0.01$  eV for density of state calculations with converged sampling of the Brillouin zone. For slabs with defects, the work function is determined with the first method with a minimum of  $10 \times 10 \times 1$  grid and the tetrahedra method for Brillouin zone

integrations; up to  $16 \times 16 \times 1$  grids were tested with differences on the order of 0.02 eV in the computed Fermi level. We note our reported work functions differ by  $\approx 1$  eV compared to Refs. 8 and 9. We find this difference is attributable to a combination of poor sampling of the Brillouin zone and for Ref. 9 also the fact that the Fermi level is taken as the valence band maximum.

Table S2: Calculated intrinsic Fermi levels for pristine slabs at standard DFT, DFT+U, and DDH levels of theory relative to the valence (VBM) and conduction (CBM) band extrema.

Method	$E_F$ -CBM (eV)	$E_F$ -VBM (eV)	$E_g$ (eV)
DFT	-0.293	1.915	2.21
$\mathrm{DFT}{+}\mathrm{U}$	-0.278	1.991	2.27
DDH	-0.331	2.903	3.44
DDH (exp structure)	-0.332	2.561	2.89

Next we present the density of states corresponding to Table 1 of the main text.

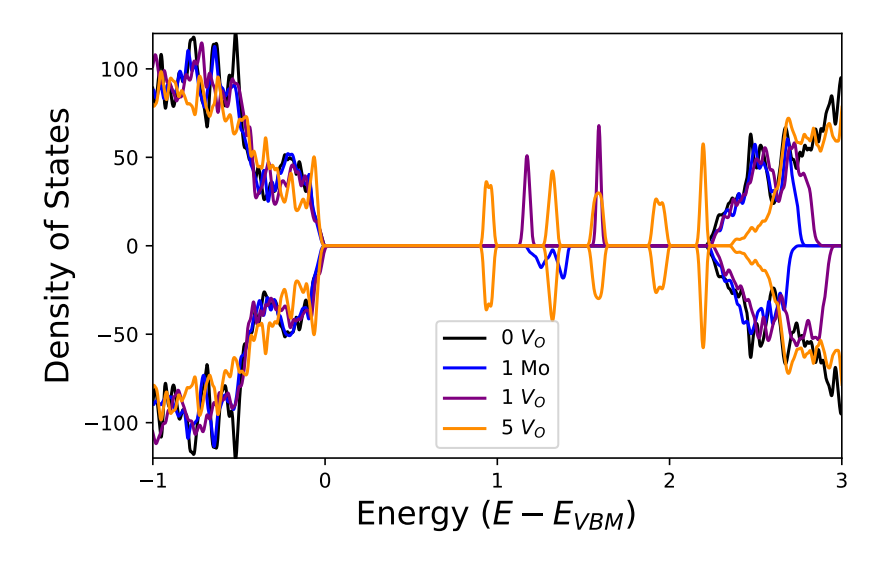


Figure S6: Density of states corresponding to calculated work functions for the pristine (0  $V_O$ , black), 1 at% Mo-doping (1 Mo, blue), 1 at% oxygen vacancy concentration (1  $V_O$ , purple), and 5 at% oxygen vacancy concentration (5  $V_O$ , orange). The valence band maximum is set to zero for each case.

#### Pristine Bulk and Surface Parameters

Our calculated lattice parameters and band gaps are summarized in Table S3 along with comparison to values in the literature. To obtain an estimate of the temperature renormalization on the band edge positions, we use a model based on Rayleigh-Schrödinger perturbation theory from Ref. 10:

$$\Delta E = \omega_{LO}[\alpha + 0.0159\alpha^2 + 0.000806\alpha^2 + O(\alpha^4)], \tag{5}$$

where  $\omega_{LO}$  is the phonon frequency of the longitudinal optical phonon and  $\alpha$  is a dimensionless coupling constant defined as

$$\alpha = \frac{e^2}{\hbar} \left( \frac{m_b^*}{2\hbar\omega_{\rm LO}} \right)^{1/2} \left( \frac{1}{\varepsilon_{\infty}} - \frac{1}{\varepsilon_0} \right). \tag{6}$$

We took the static and high-frequency dielectric constants as  $\varepsilon_0 = 52$  and  $\varepsilon_\infty = 6.9$  from Ref. 4,  $\omega_{\rm LO} = 828\,{\rm cm}^{-1}$  from Refs. 11,12, and use representative effective band masses  $m_b^*/m_0 \approx 1.5$ , calculated with a hyperbolic fit.

To obtain an estimate of the excitonic binding energy  $E_b$ , we used an effective hydrogenic model

$$E_b = \frac{\mu}{m_0 \varepsilon_{\infty}} \cdot 13.61 \,\text{eV} \tag{7}$$

where  $\mu = m_e^* m_h^* / (m_e^* + m_h^*)$  is a reduced effective mass of the electron  $m_e^* / m_0 \sim 1.5$  and hole  $m_h^* / m_0 \sim 1.5$  effective masses and  $m_0$  is the bare electron mass.

A full comparison of our calculated slab properties at standard DFT, DFT+U, and hybrid levels of theory in comparison with literature and measured values is presented in Table S4.

Table S3: Comparison of bulk lattice parameters and band gaps at standard DFT, DFT+U, and DDH levels of theory for this work and with calculated and measured literature values. Lattice parameters are reported in the I2/b space group convention. BNL indicates measurements were done at Brookhaven National Laboratory.

Method	Lattice (Å, °)	$E_g \text{ (eV)}$	Notes
DFT	a = 5.169	2.21	This work
	c = 11.773		
$\mathrm{DFT}{+}\mathrm{U}$	a = 5.172	2.27	This work
	c = 11.770		
DDH	a = 5.137	3.44	This work
	c = 11.684		
PBE	a = 5.108, b = 5.108		CASTEP <sup>a</sup>
	c = 11.522		
	eta=89.99		
PBE	a = 5.185, $b = 5.17$	2.06	$VASP^{b}$
	c = 11.79		
	$\beta$ = 90.03		
HSE06-PBEsol	a = 5.19, b = 5.073	2.41	$VASP^c$
	c = 11.68		
	$\beta = 90.21$		
XRD, electron diffraction	a = 5.19, b = 5.09		This work (BNL; epitaxial)
	c = 11.70		, - ,
	$\beta = 90.38$		
$ m LEED^d$	$c = 5.56 \pm 0.42$	2.6	
Powder neutron diff. <sup>e</sup>	a = 5.193, b=5.089		at 295 K
	c = 11.697		
	eta=90.387		
	a = 5.214, b=5.084		at 4.5 K
	c = 11.706		
	$\beta=90.394$		
$ m XRD^f$	a = 5.195, b = 5.093		
	c = 11.704		
	$\beta = 90.383$		
RIXS, UV-Vis <sup>g</sup>	•	2.52	on FTO, CVD
UV-Vis Reflectance <sup>h</sup>		2.34	on ITO, hydrotherm.
$\mathrm{PES^{i}}$		2.44	on FTO, spin coat
Photocurrent onset <sup>j</sup>		2.46	nanoporous

<sup>&</sup>lt;sup>a</sup> Ref. 13.

<sup>&</sup>lt;sup>b</sup> Ref. 14

<sup>&</sup>lt;sup>c</sup> Ref. 15

<sup>&</sup>lt;sup>d</sup> At surface; Ref. 7

<sup>&</sup>lt;sup>e</sup> Ref. 16

<sup>&</sup>lt;sup>f</sup> Ref. 17

 $<sup>^{\</sup>rm g}$  Ref. 18

<sup>&</sup>lt;sup>h</sup> Ref. 19

<sup>&</sup>lt;sup>i</sup> Ref. 20

Table S4: Calculated and measured work functions  $\varphi$ , surface energies, and conduction (CBM) and valence (VBM) band positions from vacuum level.

Method	Surf. E	$\varphi$	CBM	VBM	
	$(\mathrm{J/m^2})$	(eV)	(eV)	(eV)	
DFT	0.330	5.447	5.112	7.309	This work
$\mathrm{DFT}{+}\mathrm{U}$	0.326	5.401	5.050	7.303	This work
DDH	0.363	5.034	4.597	8.042	This work
NEXAFS, PES <sup>b</sup>	1	5.15	4.85	7.45	Czolchralski single crystal
XAS,XES,XPS <sup>a</sup>		5.27	4.79	7.27	on FTO, CVD
$XPS, UPS^{c}$		5.6 - 5.7		7.5	sputtered Mo-doped $m$ -BiVO <sub>4</sub>
					on $RuO_2$ and ITO
$XPS, UPS^d$		5.7 - 6.6			PLD $m$ -BiVO <sub>4</sub> ;
					on ITO, with $\mathrm{NiO_x}$ , $\mathrm{CoO_x}$ co-catalyst

<sup>&</sup>lt;sup>a</sup> Ref. 21.

#### Determination of chemical potentials

Limits on  $\mu_{\rm O}$  may be determined based on the stability of BiVO<sub>4</sub>:

$$\Delta H^f(\text{BiVO}_4) = \mu_{\text{Bi}} + \mu_{\text{V}} + 4\mu_{\text{O}} , \qquad (8)$$

where  $\Delta H^f(\text{BiVO}_4)$  is the enthalpy of formation,  $\mu_i$  (i = Bi,V,O) is the chemical potential of species i referenced to the constituent elements, i.e., the elemental metals and molecular oxygen.

$$\mu_{\text{Bi}} \le \mu_{\text{Bi}}(\text{Bi metal}) = 0$$

$$\mu_{\text{V}} \le \mu_{\text{V}}(\text{V metal}) = 0$$

$$\mu_{\text{O}} \le \mu_{\text{O}}(\text{O}_2 \text{ gas}) = 0$$
(9)

Competing compounds further constrain the window of chemical potentials for which

<sup>&</sup>lt;sup>b</sup> Ref. 7

<sup>&</sup>lt;sup>c</sup> Ref. 12.

<sup>&</sup>lt;sup>d</sup> Ref. 22.

 $BiVO_4$  is stable. Here, we consider  $Bi_2O_3$ ,  $VO_2$ ,  $V_2O_3$ , and  $V_2O_5$ .

$$\mu_{V} + 2\mu_{O} \leq \Delta H^{f}(VO_{2})$$

$$2\mu_{V} + 3\mu_{O} \leq \Delta H^{f}(V_{2}O_{3})$$

$$2\mu_{V} + 5\mu_{O} \leq \Delta H^{f}(V_{2}O_{5})$$

$$2\mu_{Bi} + 3\mu_{O} \leq \Delta H^{f}(Bi_{2}O_{3})$$

$$(10)$$

We additionally present a comparison of our calculated formation enthalpies, which are used to determine the window of chemical potentials for which BiVO<sub>4</sub> is stable, in Table S5.

Table S5: Calculated and measured enthalpies of formation in eV/unit cell for the phases considered in the determination of chemical potentials.

Compound	Experiment	GGA <sup>a</sup>	DFT+U b
$BiVO_4$	_	-13.95	-11.67
$\mathrm{Bi_2O_3}$	$-5.89$ $^{\rm c}$	-8.91	-5.79
$VO_2$		-8.02	-7.39
$V_2O_3$	$-12.63 ^{\rm d}$	-13.07	-13.27
$V_2O_5$	-16.07 $^{\rm d}$	-18.01	-16.14

<sup>&</sup>lt;sup>a</sup> Ref. 14.

Overall, we find that DFT+U provides a better description of the enthalpies of formation compared to those obtained with GGA.<sup>14</sup> The main discrepancy between our range of accessible chemical potentials compared to Ref. 14 is the enthalpy of formation  $\Delta H^f$  for BiVO<sub>4</sub>. The smaller  $\Delta H^f$  in this work results in a smaller region of stability for BiVO<sub>4</sub>.

The range of possible values for  $\mu_{\rm Bi}$ ,  $\mu_{\rm V}$ , and  $\mu_{\rm O}$  are shown in the shaded region of Figure S7. We select three points on the chemical potential map as representative sets of chemical potentials under different conditions, labelled as A (O poor/Bi rich), B (intermediate), C (O rich). The range of chemical potentials values shown in Figure S7 for  $\mu_{\rm Bi}$ ,  $\mu_{\rm V}$ , and  $\mu_{\rm O}$  are  $A \to (0, -3.62, -2.01)$  eV,  $B \to (-1.54, -4.64, -1.37)$  eV, and  $C \to (-3.26, -8.41, 0)$  eV. The formation energy diagram for oxygen rich conditions at point C are shown in Figure

<sup>&</sup>lt;sup>b</sup> This work.

<sup>&</sup>lt;sup>c</sup> Ref. 23.

<sup>&</sup>lt;sup>d</sup> Ref. 24.

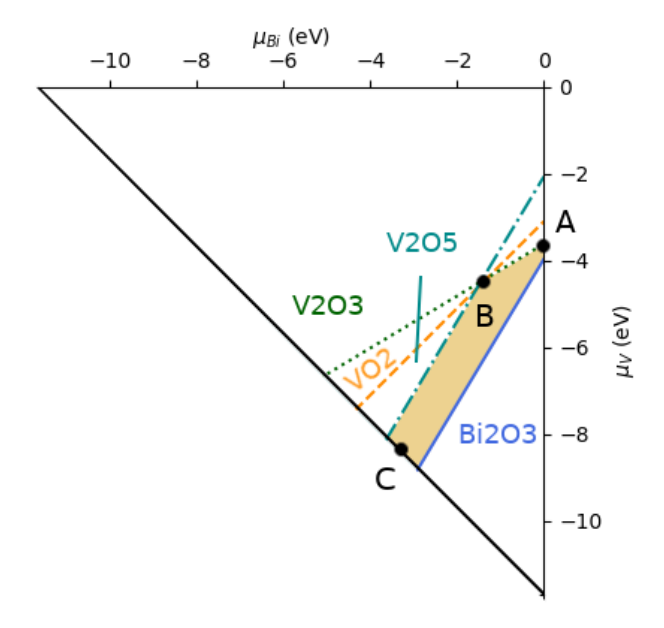


Figure S7: (Color online) Possible range of chemical potentials (yellow shaded region) for equilibrium conditions of BiVO<sub>4</sub> when considering the formation of several competing oxides as function of the V and Bi chemical potentials; the O chemical potential is fixed by the enthalpy of formation for BiVO<sub>4</sub>. Specific points are chosen as representative chemical potentials in the calculation of formation energies (see text for details.

6 of the main text. The formation energy of the oxygen vacancy for conditions at points A and B are a rigid energy shifts specified by  $\mu_{\rm O}$ .

#### References

- (1) Helander, M. G.; Greiner, M. T.; Wang, Z. B.; Lu, Z. H. Pitfalls in Measuring Work Function Using Photoelectron Spectroscopy. Applied Surface Science 2010, 256, 2602– 2605.
- (2) Kweon, K. E.; Hwang, G. S. Hybrid Density Functional Study of the Structural, Bonding, and Electronic Properties of Bismuth Vanadate. *Physical Review B* 2012, 86, 165209.
- (3) Freysoldt, C.; Neugebauer, J. First-Principles Calculations for Charged Defects at Surfaces, Interfaces, and Two-Dimensional Materials in the Presence of Electric Fields. Physical Review B 2018, 97, 205425.
- (4) Kim, T. W.; Ping, Y.; Galli, G. A.; Choi, K.-S. Simultaneous Enhancements in Photon Absorption and Charge Transport of Bismuth Vanadate Photoanodes for Solar Water Splitting. *Nature Communications* 2015, 6, 8769.
- (5) Seo, H.; Ping, Y.; Galli, G. Role of Point Defects in Enhancing Conductivity of BiVO<sub>4</sub>.
  Chemistry of Materials 2018, 30, 7793–7802.
- (6) Mostofi, A. A.; Yates, J. R.; Pizzi, G.; Lee, Y.-S.; Souza, I.; Vanderbilt, D.; Marzari, N. An Updated Version of Wannier90: A Tool for Obtaining Maximally-Localised Wannier Functions. Computer Physics Communications 2014, 185, 2309–2310.
- (7) Favaro, M.; Uecker, R.; Nappini, S.; Píš, I.; Magnano, E.; Bluhm, H.; van de Krol, R.; Starr, D. E. Chemical, Structural, and Electronic Characterization of the (010) Surface of Single Crystalline Bismuth Vanadate. The Journal of Physical Chemistry C 2019, 123, 8347–8359.
- (8) Hegner, F. S.; Forrer, D.; Galán-Mascarós, J. R.; López, N.; Selloni, A. Versatile Nature

- of Oxygen Vacancies in Bismuth Vanadate Bulk and (001) Surface. The Journal of Physical Chemistry Letters 2019, 10, 6672–6678.
- (9) Hu, J.; Chen, W.; Zhao, X.; Su, H.; Chen, Z. Anisotropic Electronic Characteristics, Adsorption, and Stability of Low-Index BiVO<sub>4</sub> Surfaces for Photoelectrochemical Applications. ACS Applied Materials & Interfaces 2018, 10, 5475–5484.
- (10) Smondyrev, M. A. Diagrams in the Polaron Model. *Theoretical and Mathematical Physics* **1986**, *68*, 653–664.
- (11) Galembeck, A.; Alves, O. L. BiVO<sub>4</sub> Thin Film Preparation by Metalorganic Decomposition. *Thin Solid Films* **2000**, *365*, 90–93.
- (12) Hermans, Y.; Klein, A.; Ellmer, K.; van de Krol, R.; Toupance, T.; Jaegermann, W. Energy-Band Alignment of BiVO<sub>4</sub> from Photoelectron Spectroscopy of Solid-State Interfaces. The Journal of Physical Chemistry C 2018, 122, 20861–20870.
- (13) Zhao, Z.; Li, Z.; Zou, Z. Structure and Energetics of Low-Index Stoichiometric Monoclinic Clinobisvanite BiVO<sub>4</sub> Surfaces. *RSC Advances* **2011**, *1*, 874–883.
- (14) Yin, W.-J.; Wei, S.-H.; Al-Jassim, M. M.; Turner, J.; Yan, Y. Doping Properties of Monoclinic BiVO<sub>4</sub> Studied by First-Principles Density-Functional Theory. *Physical Review B* 2011, 83, 115102.
- (15) Wadnerkar, N.; English, N. J. Density Functional Theory Investigations of Bismuth Vanadate: Effect of Hybrid Functionals. Computational Materials Science 2013, 74, 33–39.
- (16) Sleight, A.; Chen, H.-Y.; Ferretti, A.; Cox, D. Crystal Growth and Structure of BiVO<sub>4</sub>.
  Materials Research Bulletin 1979, 14, 1571–1581.
- (17) Cox, D.; Moodenbaugh, A.; Sleight, A.; Chen, H.- Y., Structural Refinement of Neutron

- and X-Ray Data by Rietveld Method: Application to Al<sub>2</sub>O<sub>3</sub> and BiVO<sub>4</sub>. NBS Special Publication 1980, 567, 189–201.
- (18) Cooper, J. K.; Gul, S.; Toma, F. M.; Chen, L.; Liu, Y.-S.; Guo, J.; Ager, J. W.; Yano, J.; Sharp, I. D. Indirect Bandgap and Optical Properties of Monoclinic Bismuth Vanadate. The Journal of Physical Chemistry C 2015, 119, 2969–2974.
- (19) Tachikawa, T.; Ochi, T.; Kobori, Y. Crystal-Face-Dependent Charge Dynamics on a BiVO<sub>4</sub> Photocatalyst Revealed by Single-Particle Spectroelectrochemistry. ACS Catalysis 2016, 6, 2250–2256.
- (20) Malashchonak, M. V.; Streltsov, E. A.; Kuliomin, D. A.; Kulak, A. I.; Mazanik, A. V. Monoclinic Bismuth Vanadate Band Gap Determination by Photoelectrochemical Spectroscopy. *Materials Chemistry and Physics* 2017, 201, 189–193.
- (21) Cooper, J. K.; Gul, S.; Toma, F. M.; Chen, L.; Glans, P.-A.; Guo, J.; Ager, J. W.; Yano, J.; Sharp, I. D. Electronic Structure of Monoclinic BiVO<sub>4</sub>. *Chemistry of Materials* **2014**, *26*, 5365–5373.
- (22) Hermans, Y.; Murcia-López, S.; Klein, A.; van de Krol, R.; Andreu, T.; Morante, J. R.; Toupance, T.; Jaegermann, W. Analysis of the Interfacial Characteristics of BiVO<sub>4</sub>/Metal Oxide Heterostructures and Its Implication on Their Junction Properties. Physical Chemistry Chemical Physics 2019, 21, 5086–5096.
- (23) Ganesan, R.; Gnanasekaran, T.; Srinivasa, R. S. Determination of Standard Molar Gibbs Free Energy of Formation of Bi<sub>2</sub>O<sub>3</sub> over a Wide Temperature Range by EMF Method. *Journal of Chemical Thermodynamics* **2003**, *35*, 1703–1716.
- (24) Robie, R. A.; Hemingway, B. S.; Fisher, J. R. Thermodynamic Properties of Minerals and Related Substances at 298.15 K and 1 Bar (10<sup>5</sup> Pascals) Pressure and at Higher Temperatures; U.S. Geological Survey Bulletin 1452; 1979.